An Experimental Study of Three-Dimensional Inlet Shock-Boundary Layer Interactions

by

W. Ethan Eagle

A dissertation submitted in partial fulfillment
of the requirements for the degree of
Doctor of Philosophy
(Aerospace Engineering)
in The University of Michigan
2012

Doctoral Committee:

Professor James F. Driscoll, Chair
Professor Stephen F. Ceccio
Associate Professor Luis P. Bernal
Associate Professor Aline J. Cotel
John A. Benek, Wright Patterson Air Force Base

L.F. Dubourg inv.

I. Fellorma sculp.

Don’t Panic

ACKNOWLEDGEMENTS

My thesis advisor, Jim Driscoll, thanks for adopting me and my project, for providing excellent guidance and assistance throughout my graduate career, and for putting up with the 'rabble rousing' I was fond of around the department, college and university levels. Having room to breathe allowed me to flourish and grow, and was only possible thanks to your understanding. I have learned much from your technical excellence and enjoyed even more working and traveling with you. You are a model professor, and one I hope to one day live up to. Thanks to my committee, Steve Ceccio, Luis Bernal, Aline Cotel and Jack Benek for your excellent questions and thoughtful contributions through this process. This document is much improved because of and very much thanks to your insightful input. And my gracious thanks go to the Air Force Research Lab through the Collaborative Center for Aerospace Science for funding much of my PhD.

The work at the FXB wouldn't be possible without everyone behind the scenes, and I'm thankful for such wonderful support. Without the aerospace technical staff: Dave McClean, Thomas Griffin, Eric Kirk, Chris Chartier, Aaron Borgman, and Terry Larrow, none of the experimental projects at Michigan would be as successful. Thanks to Doug Neal and Rich Prevost from LaVision for your supportive advice, especially regarding calibration and post-processing. It was only with your help that I acquired all this data. My thanks to Denise Phelps, the graduate coordinator, for her positive attitude, particularly when things are otherwise stressful, and who is always

mindful of the needs of graduate students. I am also indebted to her for gathering the department's help to win two Outstanding Student Instructor awards. Thanks to Cindy Enoch who made sure I never waited for overdue parts or purchasing orders. Thanks to graduate chairs Chair, Carlos Cesnik, and Department chairs Wei Shyy, Ken Powell, and Dan Inman for their patient ears, and financial backing during many meetings regarding grad life at Michigan. And thanks to Iain Boyd, who's excellent lab first drew my attention to Michigan.

To my many wonderful friends, I am lucky to have met you all. To the Aero Scotch Club, especially Paul Giuliano, Tim Eyman, and Adam Shabshelowitz. It may have taken two years, but I think we finally got a good social group off the ground. I hope for many more nights of good conversation and good music in the years ahead. To all the men of the Michigan Men's Glee Club, but particularly former director Paul Rardin. You are like a second family, and you accepted me as one of your own. To the first class that welcomed me, particularly Adam Clarke, Josh Sanchez, Abe Hiatt, Tim McQuade, and my 'big brother' Alex Weatherup, we had a two week trip through Europe that I'll never forget. Also, clubbers Seth Aylesworth, Mike Maddigan and Joe Wieciek, for singing with me at the Rose 'n Crown on one of the best days ever.

To my very good friend and office mate, Tyler Huismann, without whom I never would have ended up at Michigan. I wish you well on your way. To the friends who spent grad nights at trivia with me - "Hugh and the Manatees" - Katheryne Bevilaqua and John Paul Hampstead. You helped keep me sane through the long days and nights. To my close friend and fellow rabble rousers, Sakib Elahi, Dan Nathan-Roberts, Darshan Karwat, and the rest of the Epeians, we have a good thing going. Here's to another twenty-five years!

To Kristin, for being the inspiration that kept me working long nights in the lab down the stretch, and who still encourages me to always give my all. You are the best friend I've ever had and I don't know what I would do without you. I owe you greatly for teaching me about self respect, and for giving me the courage to carry my mistakes. We still have much to teach each other and experience together. May this end be also a new beginning.

To Mom, Dad, Tom, Jayne, Wiebke, Grace, Luke, Chris, and Karen, our family has taught me that if it's worth it, it's worth going the distance.

And to you, my kind reader, the rest of these pages are thankful for you.

TABLE OF CONTENTS

LIST OF FIGURES

Figure

LIST OF TABLES

Table

LIST OF APPENDICES

Appendix

NOMENCLATURE

Symbol	Description
d_p	Diameter of seed particles
F	Forces describing vortex-vortex interaction
H	Incompressible shape factor
H^*	Shape factor modified using finite integration limits
I	Intersection point between incident and reflected shock waves
Kn	Knudsen number
k	$\equiv \frac{1}{2}\left(\overline{u'^2} + \overline{v'^2} + \overline{w'^2}\right)$, Turbulence kinetic energy
L_0	Upstream penetration distance of SBLI
M	Mach number
N	Number of samples
p	Static pressure
p_0	Stagnation pressure
Re_δ	Reynolds number based on boundary layer height
Re_θ	Reynolds number based on momentum thickness
St	Stokes number
S_{ij}	Strain rate tensor
s	Centerline spacing micro-ramp array elements
T	Static temperature

T_0	Stagnation temperature
Δt	Interframe time
u	Local streamwise velocity component
U_∞	Incoming free-stream velocity
u_τ	$\equiv \sqrt{\tau_w/\rho_w}$, Friction velocity
u_n	Shock-normal velocity component
v	Local wall-normal velocity component
w	Local spanwise velocity component
x	Streamwise dimension
y	Wall-normal dimension
z	Spanwise dimension

Greek

β	Flow deflection angle
Γ	Circulation
γ	Specific heat ratio
δ	Local boundary layer thickness
δ_0	Reference boundary layer thickness at SBLI location
δ^*	Displacement thickness
$\langle\delta^*\rangle$	Net displacement thickness, using finite integration limits
δ_{ij}	Kronecker delta tensor
θ	Free stream deflection angle;
	Momentum thickness
μ	Dynamic viscosity
ν	Kinematic viscosity

ρ	Density
σ	Statistical variance
τ_f	Fluid-dynamic timescale
τ_p	Timescale for particle lag
ω	Vorticity

Mathematical

$\overline{(\cdot)}$	Ensemble averaged quantity
$(\cdot)'$	Fluctuating quantity from Reynolds decomposition
$\sim$	Proportional to

Initializations & Acronyms

DNS	Direct numerical simulation
LES	Large eddy simulation
RANS	Reynolds-averaged Navier-Stokes
SBLI	Shock/boundary layer interactions
SPIV	Stereo particle image velocimetry
LDV	Laser doppler velocimetry
3DI	Three dimensional inlet
CPT	Critical Point Theory
SFSC	Secondary Flow Separation Concept
FOV	Field of View
IW	Interrogation Window

CHAPTER I

Relevance

Techniques to measure three components of velocity have never been applied to a shock wave boundary layer interaction (SBLI) across it's entire span. Such measurements have been made at the University of Michigan 'Glass Inlet' facility to enhance conceptual understanding of three-dimensional inlet shock-boundary layer interaction (3DI-SBLI). It has long been assumed that shock wave boundary layer interaction dynamics are principally the result of axial (two-dimensional) pressure forces arising from the interaction of the adverse pressure gradient (shock) with the wall. *Instead this thesis investigates inlet SBLI as fundamentally three-dimensional in every aspect and directly measures the causes and effects of secondary interactions.*

Since principle contributions to physics based understanding of many forms of SBLI has only occurred in two dimensions, our first step will be to understand critical point theory (CPT), the model of three-dimensional separation provided by Legendre (Delery et al., 2001). A CFD accessible experimental geometry is chosen, and three-dimensionality of the interaction is confirmed through surface oil flow visualization. Combining our two-dimensional intuition with a CPT description of oil flow measurements in this experiment leads to a new hypothetical vortex flow interaction in 3DI-SBLI, called the secondary flow separation concept (SFSC). This

description supplants the traditional two-dimensional interpretation of this flow.

After reviewing the understanding of three-dimensional systems, new results from a PIV study in this SBLI are presented with particular emphasis on an inclusive three dimensional approach. This methodology was motivated by the discrepancies between predicted behavior and reality when the focus was set on one objective (measuring a 2D-SBLI) rather than a system perspective. The SFSC hypothesis predicts the presence and potential interactions of streamwise vorticity and 'vortex lines.' PIV measurements from all three orthogonal directions each substantially confirm the hypothesis.

The secondary flow separation concept indicates that the local secondary flow pattern can be used to determine the structure and character of a 3DI-SBLI. The thesis will demonstrate that assembling physically intuitive building blocks of three-dimensional flow previously described in the literature and unifying them with vorticity measurements in 3DI-SBLI, contributes a quasi-predictive framework called the three-dimensional secondary flow separation concept (SFSC) and this framework is verified to occur for our chosen flow condition. Such knowledge potentially impacts future control strategies and also prescribes the potential avenues for further development (or breakdown) of such flows.

1.1 Motivation

Better understanding of SBLI is crucial to work on next generation flight systems, including ram and scramjet inlets and is motivated by recent failures of the X-51 hypersonic flight vehicle. Recent failures clearly demonstrate a need for better prediction of complex flow behavior in high-speed devices. In particular, AFRL attributes these flight failures to 'vehicle unstart' where a shock propagates forward

from the combustor, through the inlet and ends at the nose of the vehicle. This event is principally due to shock wave boundary layer interactions creating distortion and flow blockages, the description of which is at the heart of this thesis.

That scarce attention has been paid to the effect of the sidewalls in an enclosed inlet on SBLI structure is not surprising. Simulations of traditional SBLI phenomenon often assume two dimensional flow, and often experiments occur in large aspect ratio wind tunnels where the area of interest is confined to the central third (or less) of the span. However, a two dimensional understanding of the challenges of 'unit physics' type problems is not readily translatable to real systems. Interest in validated CFD for such full three-dimensional inlets is ever increasing (e.g. the AIAA-SBLI workshop in Orlando 2010.) Though it seems that no one particular CFD method is outpacing any other (Debonis et al., 2010), the continuing lack of validation-quality experiments using simple geometries (e.g. full span, and without 'aerodynamic fences') is also a concern (Settles and Dodson, 1994).

1.2 Outline of Present Work

Chapter II briefly presents historical developments of theories related to SBLI from both experimental and computational efforts, previous PIV studies of SBLI, as well as the definitions of qualitative metrics of CPT flow separation and logical next step which leads to the theoretical hypothesis of the SFS concept. Chapter III describes the experimental facility and provides additional detail on the measurement techniques and run conditions pertinent to uncertainty analysis. Chapter IV outlines oil flow, pressure, and Schlieren data collected which indicates the need for an alternative hypothesis to a traditional two-dimensional understanding. Chapter V presents PIV data from six streamwise planes, three each in the vertical and hori-

zontal directions. The data confirm a highly three dimensional interaction structure occurs. Chapter VI presents, *for the first time,* PIV data from the ten spanwise planes imaged from the centerline all the way into the corner region of an SBLI. Using this data to compute and track streamwise vorticity confirms the ideas of the SFSC. Finally, Chapter VII contains a summary of results and conclusions and provides an outlook on future work.

1.3 Prime Objective

Previous studies of three-dimensional separated flows have suggested possible mechanisms to explain the flow field behavior in the vicinity of critical points (See §2.2). However, no studies have conclusively established the nature of the flow between critical points. In addition, no studies of internal flows using critical point concepts have been undertaken. The present investigation aims to provide a more definitive analytical framework using detailed measurement of the three-dimensional inlet flow through an oblique shock SBLI using SPIV paired with conventional oil flow experiments to explain the interaction. The quantitative nature of PIV enables a direct examination of topologies inferred by critical point theory from conventional measurement techniques and offers an opportunity to expand this analysis. Specifically, PIV measurements mate the magnitudes of the local flow structure to the oil flow topology described by critical point theory. The data indicates that secondary flows driven by vortex structures produced at primary separations (the secondary flow separation concept §2.3) successfully describe the features in this 3DI-SBLI.

CHAPTER II

Historical and New Theoretical Viewpoints

This chapter reviews previous understanding of two and three-dimensional SBLI and applications of PIV to these flows. It also traces the development of critical point theory (CPT) and, through this process, identifies several crucial gaps in the literature.

2.1 Shockwave Boundary Layer Interactions

Several comprehensive reviews of SBLI phenomenon have been compiled, most recently by Babinsky and Harvey (2011) and in previous anthologies by Adamson Jr. and Messiter (1980); Green (1970); Delery and Marvin (1986). SBLI is traditionally categorized into one of five types: normal shock, compression corner, oblique impinging shock, two crossing shocks or three-dimensional fin-plate.

2.1.1 Theories of Two- and Three-Dimensional Interactions

The first three of these five types of SBLI are characterized solely by their two-dimensional behavior. These are schematically shown in Fig. 2.1. The principle physical mechanism occurring in a two-dimensional SBLI, a boundary layer 'free interaction', was first described by Chapman et al. (1957). The interaction depends on

a threshold pressure gradient strength which is determined through the length scale of the interaction, L_0, and the overall pressure rise imposed by the shock strength, M_0, normal to the wave in the boundary layer, δ_0.

The shock wave brings with it a strong pressure rise, which propagates upstream of the inviscid impingement point in the subsonic boundary layer. The adverse pressure gradient thickens or even separates the oncoming boundary layer, and this boundary layer thickening produces the compression waves which coalesce upstream of the shock foot.

SBLI studies of the two-dimensional compression corner dominate the literature, the majority of which note the use of 'end plates' to ensure transverse disturbances are prevented from interfering with the two-dimensional interactions. However comparing two-dimensional experiments of different types continues to defy collapse to a universal scaling by Re_δ, or M_0, all while hinting at the influence of geometric three-dimensional effects. Lapsa (2009) notes that despite no one predictive theory, general trends in the data for two-dimensional interactions are available at fixed Reynolds number Re_{δ_0}:

- Separation length normalized by the boundary layer thickness, L_0/δ_0, increases with wedge angle θ for fixed M_0.
- L_0/δ_0 decreases with M_0 for fixed θ.
- The "incompressible" shape factor H is the appropriate characterization of the incoming boundary layer for scaling of the upstream interaction length L_0.

This intuitive understanding has guided much of the work on SBLI control discussed in § 2.1.4

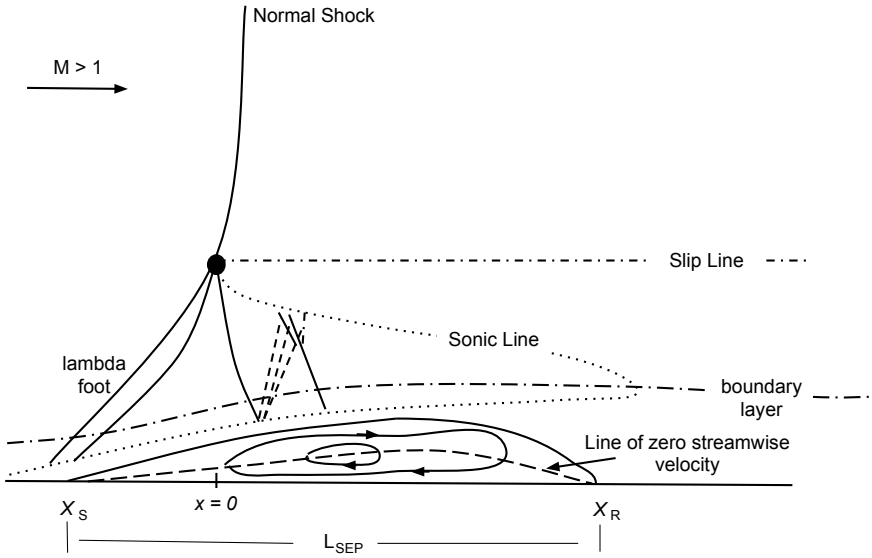

(a) Normal Shock

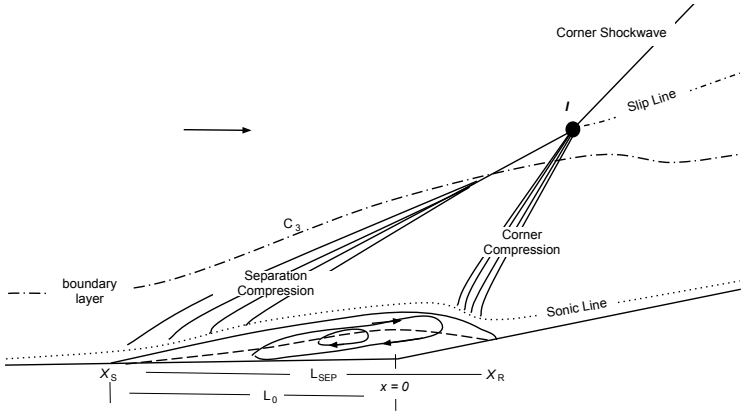

(b) Compression Corner Shock

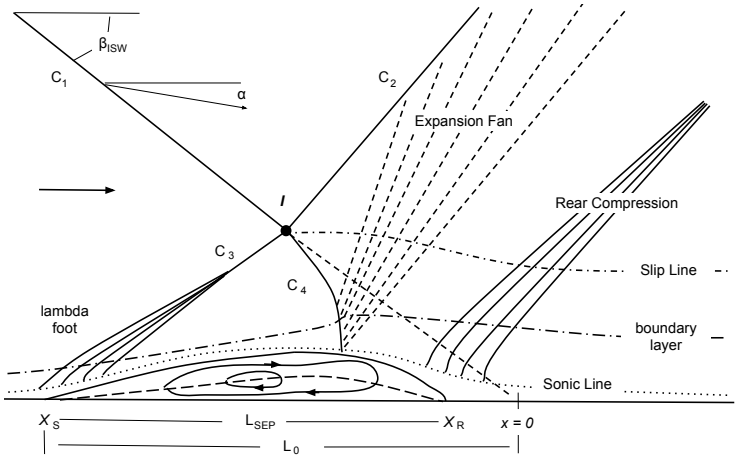

(c) Oblique Shock

Figure 2.1: Two-dimensional SBLI shock structure.

Owing to the difficulty in resolving three velocity components with traditional hot-wire and other invasive probe techniques, researchers relied on qualitative visualization methods to describe three-dimensional flows (Gadd et al., 1954; Kubota and Stollery, 1982; Mee et al., 1986; Doerffer and Dallmann, 1987; Alvi and Settles, 1992). While consensus has been drawn regarding Chapman's description of the general dynamics of various two-dimensional SBLIs that appear in Fig. 2.1 we still lack a universalizing analytical scaling for the separation length in a generalized 2D interaction.

Searching for a three-dimensional framework for SBLI leads to the other two types, a fin-plate or crossing-shock interaction. The former has been well characterized by several authors (Korkegi, 1973; Kubota and Stollery, 1982; Lu, 1983; Lu and Settles, 1990, 1991; Alvi and Settles, 1992; Schmisseur and Dolling, 1992). In particular, these authors note that the fin-plate interaction is characterized by a vortex structure under the shock foot which grows with downstream distance producing a quasi-conical interaction structure. This concept is reproduced in Fig. 2.2. The most recent work in fin-induced interactions by Dou et al. (2006) addressed the issues of separation in the swept interaction. They found that wall limiting streamlines behind the shock wave align with one ray from the virtual origin as the strength of shock wave increases. An incipient separation line is formed when the wall limiting streamline becomes perpendicular to the local pressure gradient. Since the pressure gradient is imposed by the local shock structure, this is equivalent to an alignment between the surface shear stress and the inviscid shock.

The work of a single fin interaction in the 70's, 80's, was followed by work through the 90's and into the 2000's in crossing shocks produced by two fins, or by dual cones with a flat plate boundary layer (Knight et al., 1986; Ketchum et al., 1989;

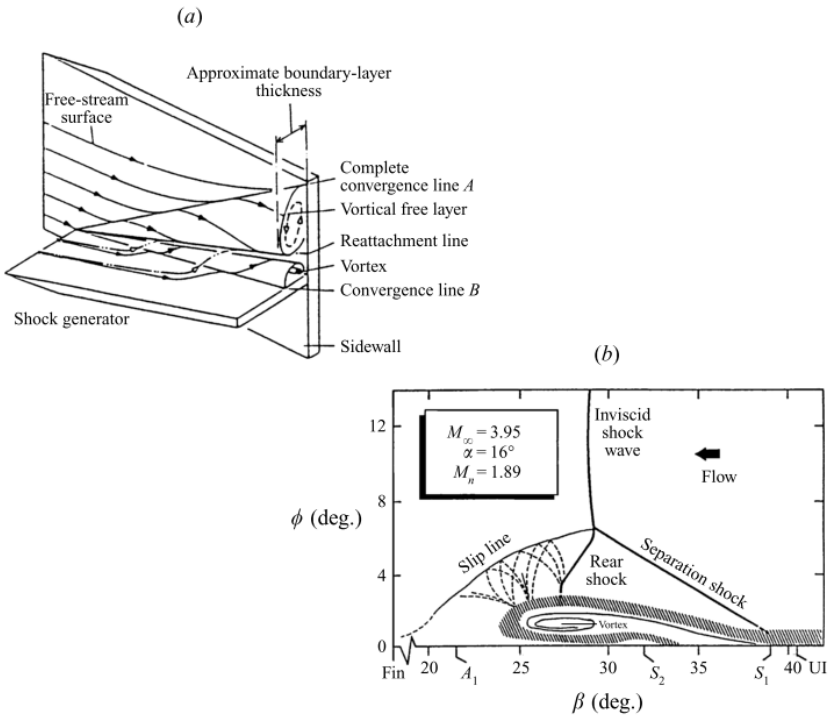

Figure 2.2: Fin-Plate SBLI (a) three-dimensional picture representation (b) Two-dimensional view orthogonal to the inviscid shock from Alvi and Settles (1992)

Narayanswami et al., 1991; Hingst and Williams, 1991; Knight et al., 1995; Zheltovodov et al., 2001; Derunov et al., 2008). Knight et al. (1986) is the first work on three-dimensionality which adopts ideas about topological flow considerations in the interaction structure and identifies CPT as a suitable approach. However, this method of investigation was never extended to traditional two-dimensional configurations.

2.1.2 Previous PIV Studies

The first ever PIV study connected to SBLI phenomenon was the PhD work of Steve Beresh under the direction of Noel Clemens and Dave Dolling (Beresh, 1999). He provided extensive experimental evidence of low frequency motion in the shock foot of an unswept compression ramp correlated to velocity fluctuation in the inner part of the boundary layer (Beresh, 1999). He collected data from ∼1500 vector fields for four seeding configurations with a final vector spacing of $2\,mm \times 2\,mm$ in a $19\,mm$ boundary layer upstream of a compression corner . The particle time constant for TiO_2 however was a relatively slow $54\mu s$ compared to the flow time scale $\delta/U_\infty = 25\mu s$. This PIV study did not measure the velocity field through the interaction. Instead it focused on the velocity in the boundary layer upstream, and correlated the motion of the shock foot (the shock foot motion is based on the location of a wall pressure rise along a series of streamwise taps) with these fluctuations.

The next PIV study of SBLI was by Hou, Clemens, and Dolling in 2003, looking at a wide field ($86\,mm \times 21.6\,mm$) ahead of the same compression ramp at Mach 2 (Hou et al., 2003). Data was collected in streamwise vertical planes along the tunnel centerline. Hou uses conditional averaging to show that upstream shock

motion lengthens the recirculation zone and is a result of velocity fluctuation in the upstream boundary layer. His result suggests that the assumption of separation occuring directly at the shock foot is misleading in the compression ramp case.

The next series of PIV measurements to arrive came out of France in 2005 and were reported by Dupont and Debieve (Dupont et al., 2005). Again, the use of PIV is mainly to determine the space/time organization of the flow field to determine properties of unsteadiness appearing in the separated zone. Each plane is visualized in 6 streamwise horizontal planes from 1 to 10mm ($\delta_0 = 11mm$) and 500 velocity fields are acquired at each plane. This study is the first to present data off centerline. The streamwise extent of the reversed flow region is 71mm and the spanwise measurement extends 35mm on either side of the centerline capturing the central 40% of the tunnel span. This view plane provides the first data on three-dimensionality in an SBLI. Solid body rotation is observed in the PIV data at 1mm from the wall for a 9.5 degree deflection but not for the 8 degree case. This data set produced a number of other good studies of unsteady effects (Dussauge et al., 2006; Dupont et al., 2008; Hadjadj and Dussauge, 2009), however unsteadiness is not the central focus of this work.

Also in Europe around that time, at the Delft Institute of Technology, a series of PIV studies of SBLI also was underway. Humble et al. (2006) present the first fluctuating quantities in the vertical direction as well as profiles of the Reynolds stress, $\overline{u'v'}$. However, given the relatively large interrogation window sizes (2mm x 2mm) compared to the particle displacements, some of these fluctuations are likely due to particle lag effects in the seeding distribution through the deceleration in the shock wave. In addition, the fluctuations (large measured Reynolds stresses) imply the generation of convected vortical structures present in the boundary layer. This

work also produced another archival paper Humble et al. (2007) which confirmed the flow particle response time, and discussed the intermittency of the reverse flow seen for the 8 degree deflection angle.

Back in the US, Ganapathisubramani et al. (2007) continued to work on compression ramp SBLI, now using streamwise horizontal image planes, again to detect the presence of unsteadiness in the shock motion. They deduced that alternating regions of high and low momentum fluid are responsible for the shock motion.

By 2008, a new PIV study came out of the Scarano/Oudhousen group (Louis et al., 2008). This time, dual-PIV provided information on turbulence correlations at previously unavailable temporal resolutions. Although not time resolved, the dual PIV system provides time delays between images in the $5\mu s$ to $2000\mu s$ range which lead to an equivalent frequency response of 200kHz to 500Hz. They confirm low frequency motion of the shock foot behavior below the frequencies of turbulence in the incoming boundary layer. However, their analysis cannot account for the spatial frequencies associated with low speed and high speed streak behavior.

The most recent study of 2D-SBLI was the predecessor to the current work by Lapsa and Dahm (Lapsa, 2009; Lapsa and Dahm, 2010). These extensive studies over three shock wave strengths measurements of the boundary layer character showed the effectiveness of SBLI passive control strategies. However, since the study focused on the central 15% of the boundary layer (approximately one passive device width) only limited claims can be made about the over-all effectiveness of these devices.

Tables 2.1 and 2.2 list the previous PIV studies; in particular, note the lack of spanwise extent of either the shock generator or the measurement location. Thirty-five percent of span is the largest spanwise extent of these previous studies. Each of these attributes contribute to making the data sets poor candidates for three-

Author	Beresh 1999	Hou 2003	Dupont 2005	Humble 2006
Mach	5 (750 m/s)	2 (497m/s)	2.3 (550 m/s)	2.1 (506 m/s)
$\frac{WidthMeasured}{TunnelWidth}$	$\frac{1mm}{152mm} =< 1\%$	$\frac{1mm}{152mm} =< 1\%$	$\frac{60mm}{170mm} = 35\%$	$\frac{4mm}{280mm} = 1.5\%$
Δt	$1.2\mu s$	$1\mu s$	$1\mu s$ - $6\mu s$	$2\mu s$
Particle time constant	$54\mu s$	2.6 μs	No Report	$2.1\mu s$
Flow time scale δ/U_∞	$25\mu s$	$26\mu s$	$20\mu s$	$38\mu s$
resolution[mm^2]	2x2	0.72 x 0.72	2.2 x 1.1	1.9 x 1.6
vector spacing	64x64 (50%)	32x32	No Report	21x17 (75%)
configuration	boundary layer	90% CR	Full Span OS	40% Span Oblique
orientation	Vertical CL	Vertical CL	6 Horizontal	5 Vertical
number of vector fields	1500	2100	500	1500
validation method	Pitot	None	LDV	None
quantities presented	$\overline{u}$, $\sqrt{\overline{u'^2}}$	$\overline{u}$, $\sqrt{\overline{u'^2}}$	$\overline{u}$, $\sqrt{\overline{u'^2}}$	$\overline{u}$, $\sqrt{\overline{u'^2}}$ $\sqrt{\overline{v'^2}}$, $\overline{u'v'}$

Table 2.1: Previous SBLI-PIV studies(1999-2006)

dimensional computational fluid dynamics (CFD) validation.

In addition to the PIV studies of two-dimensional shock boundary layer interactions, two studies on three-dimensional SBLI have previously been undertaken. The first focused on the centerline of an oblique shock reflection. They used a 70mm shock generator in a 280mm tunnel and measured the central 40mm using tomographic PIV (Humble et al., 2009). They determined that low speed streaks in the instantaneous images produce 'upsweep' in the interaction region and are the clearest precursor to flow separation.

The study of three-dimensional effects by Helmer (2011) provides the first evidence that radically different behavior occurs near the sidewalls in such interactions. However, due to limited optical access, only data from streamwise planes are presented. Thus, inferences about the overall flow structure cannot be conclusively drawn. Table 2.3 summarizes the PIV parameters of these two early contributions to three dimensional understanding.

Author	Gana... 2006	Souverein 2008	Lapsa 2009
Mach	2 (510m/s)	1.69 (448 m/s)	2.75 (600m/s)
% Width Measured	$\frac{38mm}{152mm} = 25\%$	$\frac{2mm}{280mm} =< 1\%$	$\frac{8mm}{57mm} = 14\%$
Δt	$2\mu s$	$1.5\mu s$	0.4 μs
Particle time constant	$2.6\mu s$	No Report	5.5 μs
Flow time scale δ/U_∞	$26\mu s$	$38\mu s$	$17\mu s$
resolution[mm^2]	1.28x1.28	0.43 x 0.43	0.24 x 0.24
vector spacing	32x32(50%)	31x31(75%)	32x32 (50%)
configuration	Ramp	Oblique	60% Span Oblique
orientation	Horizontal	Streamwise	Transverse and centerline
number of vector fields	750	250 - 4000	1500
validation method	None	High-Res PIV	Repeatability
quantities presented	$\overline{u}$, $\sqrt{\overline{u'^2}}$	$\overline{u}$, $\sqrt{\overline{u'^2}}$	$\overline{u}$, $\overline{v}$,$\overline{w}$, $\overline{\omega}_z$, $\overline{\omega}_x$, $\overline{S}_{yy}$, $\overline{k}$, H

Table 2.2: Previous SBLI-PIV studies(2006-2011)

Author	Humble 2009	Helmer 2011
Mach	2.1 (510m/s)	2.05 (524m/s)
% Width Measured	$\frac{14mm}{280mm} = 14\%$	Inside sidewall BL
Δt	2 μs	$0.8\mu s$
Particle time constant	2.6 μs	$4.4\mu s$
Flow time scale δ/U_∞	40 μs	$10.3\mu s$
resolution[mm^2]	Tomo - 2.1x2.1x2.1	0.135 x 0.135
vector spacing (overlap)	42x42x42 (75%)	16x16
configuration	Full Span Ramp	Full Span Ramp / Oblique Shock
orientation	Horizontal	4 Vertical
number of vector fields	750	200+
validation method	None	None
quantities presented	inst. u,v,w, $\|\omega\|$	$\overline{u}$,$\overline{v}$, $\sqrt{\overline{u'^2}}\sqrt{\overline{v'^2}}$, $\overline{u'v'}$

Table 2.3: Previous '3D' SBLI-PIV studies(2009-2011)

Global parameters defining SBLI remain elusive. The present work is part of a greater collaborative effort to enhance the understanding and prediction of SBLI. Much prior work exists on the prediction of these flows. Past and current simulation results will be briefly reviewed next to point out the need for fully three-dimensional data. Despite more than 70 years of investigation into these phenomena, the practice of two-dimensionalizing interactions is still commonplace. The assumption is that complications arising from a fully three-dimensional analysis come at a higher conceptual cost than the benefits such analysis provides. However, as the next section will demonstrate, the field is reaching the practical limits that such practice imposes on the analysis. Full field data contained herein provides the means for validation of computational models of three-dimensional SBLI.

2.1.3 Computational Efforts

Until very recently the majority of computational studies have focused on predicting two-dimensional interactions with limited (or periodic) spanwise boundary conditions (Garnier, 2009). However, the interesting and complicating aspects of computational fluid dynamics (CFD) validation are approaching their limits when uncertainty limits on primary error sources are accounted for. This means that the next level of advance for CFD SBLI requires an assessment of secondary influences on the interaction. However a comprehensive list of secondary influences is an order of magnitude larger than the primary influences due to numerous potential combinations. Placing 'blame' for differences between CFD and experiment on any one source is difficult. Yet accurate predictive tools for even canonical SBLI configurations are hampered by compressibility effects, unsteadiness, and the large range of

scales (owing to high Reynolds numbers) typically associated with these high-speed flows.

Owing to their ubiquitous industrial applications, Reynolds-averaged Navier-Stokes (RANS) approaches constitute the majority of simulations. However, the vast majority of these make use of the Boussinesq "gradient transport" hypothesis, in which the RANS equations are closed by linearly relating the Reynolds stress components to the mean strain rate tensor via an "eddy viscosity." The discrepancies with existing data are large and the errors fundamental, particularly in non-equilibrium flows when flow undergoes rapid straining though a shock wave. Even an ideal mean-field solution from a RANS simulation, however, fails to capture the fluctuating behavior of SBLI and the large dynamic loads that are caused by them. Large Eddy Simulations (LES) of flows at moderate Reynolds numbers have been reported and reviewed in the literature (Edwards, 2008). These schemes must balance numerical dissipation near shock structures against artificially damping turbulence fluctuations. This constraint mandates a dynamic subgrid model for accurate SBLI simulation.

Rarer and typically low Reynolds number, direct numerical simulations (DNS) solves the Navier-Stokes equations directly at all relevant scales of the flow. Only a few studies of canonical SBLI configurations have been computed. Muppidi and Mahesh (2007) and Wu and Martin (2007) are notable examples of DNS simulations of compression ramps, while Pirozzoli and Grasso (2006) and Ringuette et al. (2007) provides essentially the only study of incident oblique SBLI using DNS.

RANS, DNS, and LES all play important roles in the design and research communities, however the challenges presented by SBLI render none of them independently sufficient for design purposes or even for insight to basic physical understanding.

The high local strain rates, unsteady nature, and potential for reversed flow lead to considerable errors in the current RANS models. The high Reynolds numbers and resulting large range of turbulence scales make DNS impractical for all but low Reynolds number test cases. A combination of these factors also present challenges to LES, the models for which remain a research topic even outside of SBLI.

The previous study by Lapsa (2009) provided high-fidelity measurements of the quantities on which the models are based i, including the velocity, higher-order fluctuations, and gradient quantities. However, larger errors resulting from misalignment of shock impingement and reflection locations and other details of the full three-dimensional interaction has lead to the understanding that "to get it right, you have to get it all right." Such full field data until now has been unavailable.

2.1.4 Unsteadiness and Control

Boundary layer devices designed for flow control have previously been based on two-dimensional principles of SBLI. In a two-dimensional interaction, the primary control strategy is improve the 'health of the boundary layer' by pulling high momentum fluid close to the wall to prevent dramatic flow separations. Active methods are quite successful with boundary layer suction being the most common method of inlet SBLI control (Fukuda, 1977; Harloff and Smith, 1996). Recent efforts to supplant bleed with 'micro'-ramps, sub-boundary layer scale devices designed to energize portions of the boundary layer, have demonstrated some success. The secondary separation concept in §2.3 may serve as a practical guide for placing these devices; however, unsteadiness and control are not a focus of this research. Instead the test program is aimed describing the three-dimensional flow field and at producing a benchmark

data set enabling CFD validation.

2.1.5 Corner Influence

Three-dimensionality in corners of enclosed interactions was long noted but often ignored (Green, 1970). Aside from two short considerations of these effects by Reda and Murphy (1973a,b) general scholarship on the effect of end walls on SBLI has been scarce until recently. Bruce et al. (2011) provides the first experimental investigation into the influence of perturbations in the corner to the centerline behavior in a normal shock SBLI. He describes the dramatic effect that corner perturbations can have on the response of the boundary layer at the centerline, with large corner separation helping to prevent centerline separation and small corner separations aggravating separation at the centerline.

The range of corner flow SBLIs possible in the Michigan facility are described in a previous work (Eagle et al., 2011). This investigation provided the experimental experience necessary to settle on the current experimental geometry and helped direct the placement of the PIV data planes.

Another recent PIV investigation by Helmer (2011) of a sub-boundary layer scale compression corner and oblique shock reflection also notes significant three-dimensionality in the sidewall boundary layers. He describes the appearance of additional shock structures as the sidewall boundary layer is approached but does not provide an explanation other than proximity to the sidewall for this behavior.

While investigation on ninety-degree corner-flow SBLI is somewhat scarce, literature on theoretically predicted and experimentally observed generalities of corner flows over a range of speeds spans several decades (Loitsianskii et al., 1951; Gess-

ner and Jones, 1961; Libby, 1966; Watson and Weinstein, 1971; Ghia, 1975; Mojola, 1976; Davis and Gessner, 1989) and includes some very recent computational efforts (Bottaro et al., 2006; Wedin et al., 2009; Alizard et al., 2009, 2010). The relevance of ninety-degree corners to critical point theory has not been previously investigated.

Corner influence is largely ignored because analytical techniques for SBLI consider the streamwise gradients to be the controlling parameter of a localized interaction. For example, a pseudo-two-dimensional interaction was assumed to be occurring on the centerline and relative spanwise uniformity was confirmed in a region that occupied $\pm 10\%$ of the tunnel width (Lapsa, 2009). Valid and interesting dynamics were uncovered involving the turbulence interaction through the shock wave, and the relative influence of several passive SBLI control strategies were investigated. However, this assumption of two-dimensionality is called into question by Bruce et al. (2011) who elucidated the role of the corners respective to the wind tunnel aspect ratio, and demonstrated clearly that definitions of separation at the centerline are dependent on the full three-dimensional interaction profile. Thus, any explanation related to the effectiveness of control strategies for SBLI must similarly take into account fully three-dimensional effects.

2.2 Critical Point Theory

Understanding three-dimensional interactions, which are notoriously difficult to visualize, requires a simplified conceptual framework which can replace and extend traditional two-dimensional understanding of SBLI. Three-dimensional external flows have been successfully described using a framework called the critical point theory (CPT) introduced by French researcher Robert Legendre as an extension of the ideas put forth by Poincare on the structure of continuous vector fields (Legendre, 1956).

The hypothesis is simple: The surface of a body should consist of a continuous vector field, such that from any one point, there should pass one and only one trajectory. This assumption is reliable for both instantaneous and time averaged flow fields. While his work appears in textbooks and it's history and application have been thoroughly reviewed by Delery et al. (2001), the original work is not (yet) available in an English translation.

The key results describing the utility of CPT were reintroduced in a thorough analysis of the topology of three-dimensional separated flows (Tabak and Peake, 1982). They beautifully summarize previous attempts to categorize flow separation in terms of topological fluid concepts, and their remarks will be reviewed and expanded upon here. Separation occurs in one of two hypothesized flow separation structures, arising from a particular arrangement of critical points described in detail in §2.2.2. Their figures are reproduced in Fig. 2.3.

Other previous work on applications of CPT to fluid flows is available in the reviews of Perry and Chong (1987) and Moffatt et al. (1990) and is discussed briefly by Cantwell (1981). In particular, the ideas have been applied to three-dimensional separation occurring on delta wings, in channel flows, as well as for flow away from surfaces such as the critical points that occur near separation bubbles, and in jets and wakes. Surface flows in those instances were combined with qualitative flow visualization; however, unsteadiness, vortex breakdown, and turbulent mixing in the flow fields precluded a thorough confirmation of the connection between the surface flows and some (conditionally) average flow velocity. Conditional averaging was applied by Cantwell (1981) to describe the velocity field in turbulent spots.

Definitions of key terms are needed to understand the critical point framework. Turning to traditional understanding of flow separation and following the work of

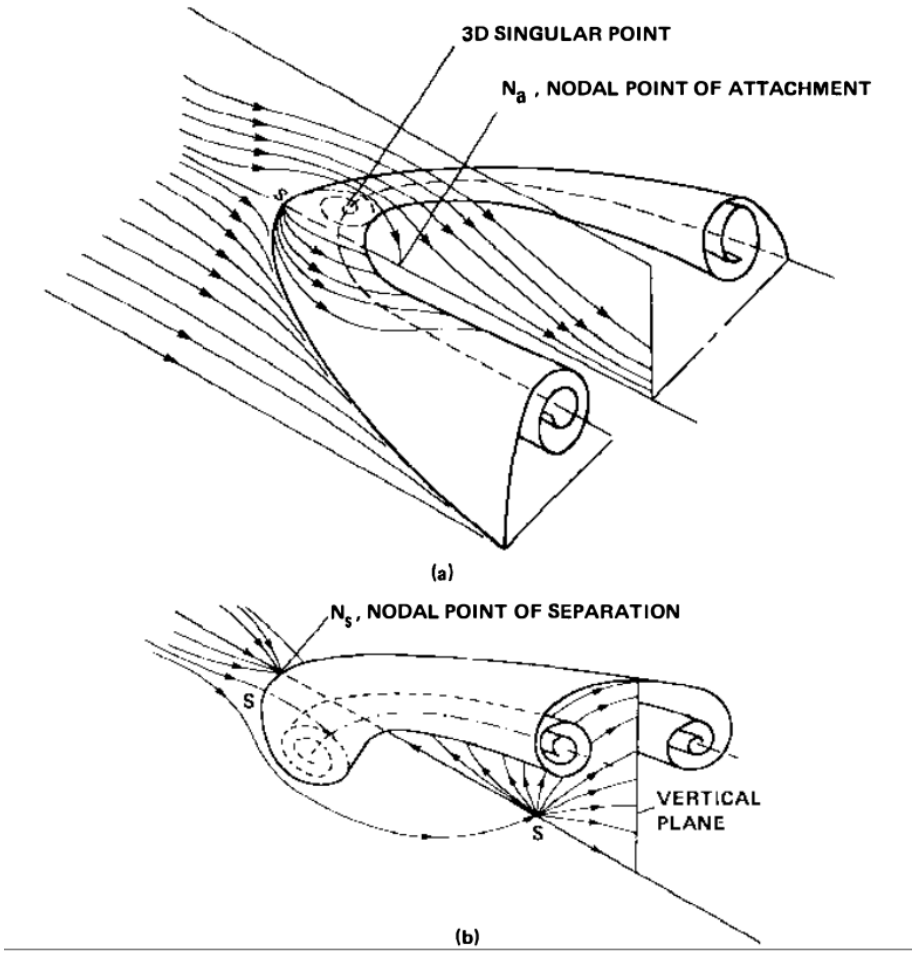

Figure 2.3: Two arrangements of three-dimensional flow separation from a flat plate (Tabak and Peake, 1982).

Delery et al. (2001) we must first consider the local skin friction.

2.2.1 Skin Friction

In a two-dimensional context, separation is defined at a point $\mathbf{p}(x, y)$ as

$$\tau_w(x) = \mu \frac{\delta u}{\delta y}(x, 0) = 0 \tag{2.1}$$

where τ_w is the local skin friction and (u, v) is a two-dimensional velocity field. However, a key difference between two and three-dimensional separations depicted in Fig. 2.4 is that a velocity component can develop in three-dimensional separation to allow flow to escape laterally; thus, flow is no longer enclosed by the region of recirculation. Considering three-dimensional separations of this type requires differentiating between open and closed separation. In a two-dimensional framework, the only type of separation considered is the closed type, where a small pocket of fluid 'recirculates' in closed streamlines, separated from the bulk flow by the separation streamline which defines the point of separation and reattachment. In the open type separation, the streamline along a two-dimensional cut never reattaches and instead the flow that turns upstream comes from out of plane, swept into the interaction by the action of vorticity. Thus, Délery suggests, two-dimenaional notion of 'reattachment' should be replaced with 'attachment' to signify that the flow leaving the surface and the flow attaching to the surface are rarely the same.

Following this lateral fluid motion, the local skin friction takes the vector form:

$$\tau_w(x, z) = \begin{pmatrix} \tau_x \\ \\ \tau_z \end{pmatrix} = \mu \begin{pmatrix} \dfrac{\delta u}{\delta y}(x, 0, z) \\ \\ \dfrac{\delta w}{\delta y}(x, 0, z) \end{pmatrix} \tag{2.2}$$

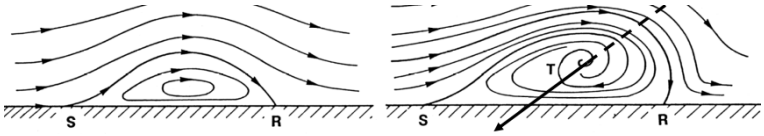

Figure 2.4: Streamlines above two and three-dimensional flow separations from "Separation in Three-Dimensional Flow" - http://www.onera.fr/conferences-en/3-separation/

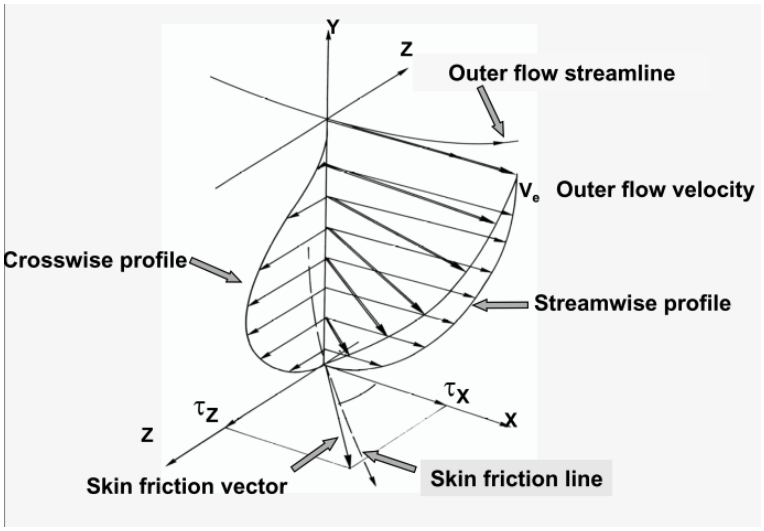

Figure 2.5: Three-dimensional flow and the local skin friction from "Separation in Three-Dimensional Flow" - http://www.onera.fr/conferences-en/3-separation/

and we define a skin friction line as a line everywhere tangent to the local skin friction vector. An example is shown in Fig. 2.5.

If the fluid is Newtonian, the concept of a 'limiting streamline' exists, in which the skin friction line is the limit of a streamline as the distance to the wall approaches zero. However, limitations to the 'streamline' approach in regions of flow separation indicate that the skin friction vector provides a more robust physical picture.

Just like a streamline in two-dimensional flow, the trajectories of the skin friction field can be defined as solutions to a simple differential equation as follows:

$$\frac{dx}{\tau_x(x,z)} = \frac{dz}{\tau_z(x,z)} \tag{2.3}$$

Thus, when a viscous oil is deposited on a wall, it flows along local skin friction lines.

2.2.2 Critical Points

As stated in §2.2.1, CPT assumes that at any given point on a body, only one skin friction lines passes through. The only exception is at points where the values of τ_x and τ_z vanish simultaneously. These are the critical points of the system. The solution, from Delery et al. (2001), depends on a Taylor expansion (first order) of Eqn. 2.3 and the solution to the associated eigenvalue problem in Eqn. 2.6;

$$\frac{dx}{\frac{\delta\tau_x}{\delta x}x + \frac{\delta\tau_x}{\delta z}z} = \frac{dz}{\frac{\delta\tau_z}{\delta x}x + \frac{\delta\tau_z}{\delta z}z} \tag{2.4}$$

Assuming derivatives are non-zero then this equation can be solved using a logarithmic form in two unknowns:

$$\begin{aligned} \frac{\lambda dx + \mu dz}{\lambda\left(\frac{\delta\tau_x}{\delta x}x + \frac{\delta\tau_x}{\delta z}z\right) + \mu\left(\frac{\delta\tau_z}{\delta x}x + \frac{\delta\tau_z}{\delta z}z\right)} &= \\ \frac{d(\lambda x + \mu z)}{S(\lambda x + \mu z)} = \frac{df}{Sf} &= -dt \\ \Rightarrow f &= Ae^{(-St)} \\ \lambda x + \mu z &= Ae^{(-St)} \end{aligned} \tag{2.5}$$

which is valid so long as the following homogeneous algebraic system can be solved for eigenvalues S1 and S2.

$$\begin{aligned} \begin{vmatrix} \frac{\delta\tau_x}{\delta x} - S & \frac{\delta\tau_z}{\delta x} \\ \frac{\delta\tau_x}{\delta z} & \frac{\delta\tau_z}{\delta z} - S \end{vmatrix} &= 0 \\ S^2 - S\left(\frac{\delta\tau_x}{\delta x} + \frac{\delta\tau_z}{\delta z}\right) + \frac{\delta\tau_x}{\delta x}\frac{\delta\tau_z}{\delta z} - \frac{\delta\tau_x}{\delta z}\frac{\delta\tau_z}{\delta x} &= 0 \end{aligned} \tag{2.6}$$

Substituting notation in Eqn. 2.6 from Delery et al. (2001), $S^2 + pS + q = 0$, the eigenvalues, S_1 and S_2 found around the critical point determine the type of solution which can be either a node, a saddle point, or a focus. These configurations are shown in Fig. 2.6. Two real positive eigenvalues indicate a node. Two conjugate or

pure imaginary eigenvalues generate a focus. Two real eigenvalues of opposite sign indicate a saddle point. The path of the skin friction around each of these give an indication of the physical significance of each.

The nodal point is common to an infinite number of skin friction lines. At a nodal attachment, all skin friction lines are directed away from the node, while at a point of separation they are all directed toward it. A focus is similar to a node in that it collects an infinite number of skin friction lines. However skin friction lines at a focus spiral around the singular point, again trajectories run away from it in the case of attachment and towards it in the case of separation. At a saddle point, only two skin friction lines pass directly through. Trajectories along one line collect the elements on either side towards the critical point while the trajectories on the second line run away from the critical point. Interestingly, these two lines act as uncrossable barriers in the skin friction field and are called 'separation' or 'attachment' lines depending on the velocity field (Tabak and Peake, 1982).

In addition, the number of critical points on a surface must follow a topological rule depending on the body. For a convex shape like a sphere, the number of nodes and foci must exceed the number of saddle points by two (Tabak and Peake, 1982). They also describe how to extend the surface flow arguments into the flow field itself. Thus surface flows can be attributed to streamline flow topologies as shown in Fig. 2.7. Using this topological framework, a flow is considered separated if the skin friction pattern contains one or more saddle points and the skin friction line leaving from this saddle point is called a 'line of separation.' According to Tabak and Peake (1982) the appearance of a new critical point in the flow causes a global separation because it alters the topological structure of the flow. However any 'line of separation' issuing from a saddle point is only a local separation.

Tabak and Peake (1982) also prove that the surface shear and surface vorticity are everywhere orthogonal. Thus the skin friction lines and the trajectories of vortex paths form a family of orthogonal curves which share critical points. As a result skin friction lines can be used to infer the trajectories of vortex lines in the vicinity of the critical point. This result is the foundation of the next section, the Secondary Flow Separation Concept. However, before moving on, we will examine the flow pattern in Fig. 2.8 to make use of CPT framework to create Fig. 2.9.

1) Inspect the skin friction line pattern to identify the critical points.

2) Draw the separation lines, identify detachment and attachment lines.

3) Make sure the surface pattern is topologically consistent; such that skin friction lines originate at a node and terminate at nodes or foci. (Such a procedure may necessitate invention of critical points not readily visible in oil flow.)

4) After this inspection, hypothesize an outer flow vortical structure consistent with (orthogonal to) the skin friction lines.

5) Attempt to validate the vortical structures in projected planes of the interaction. Do not forget fundamental theorems: A vortex cannot originate nor terminate within the flow, it closes on itself or extends to infinity.

2.3 Secondary Flow Separation Concept

Previously, critical point theory has been used as a descriptive, rather than prescriptive, theory mainly because there is no one flow field that maps to a series of skin friction lines, but instead a family of such topologies. Given that the eigenvalues in

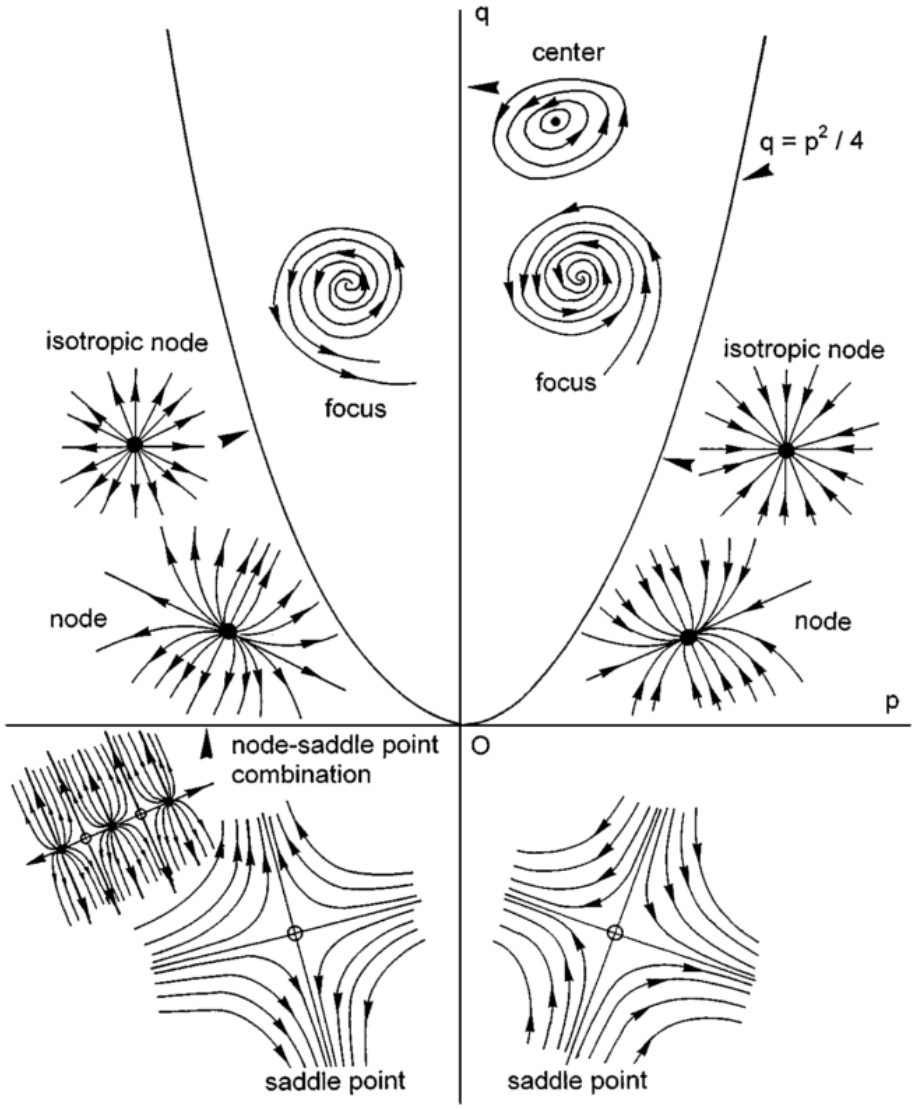

Figure 2.6: Flow topologies described by a combination of eigenvalues, from Delery et al. (2001).

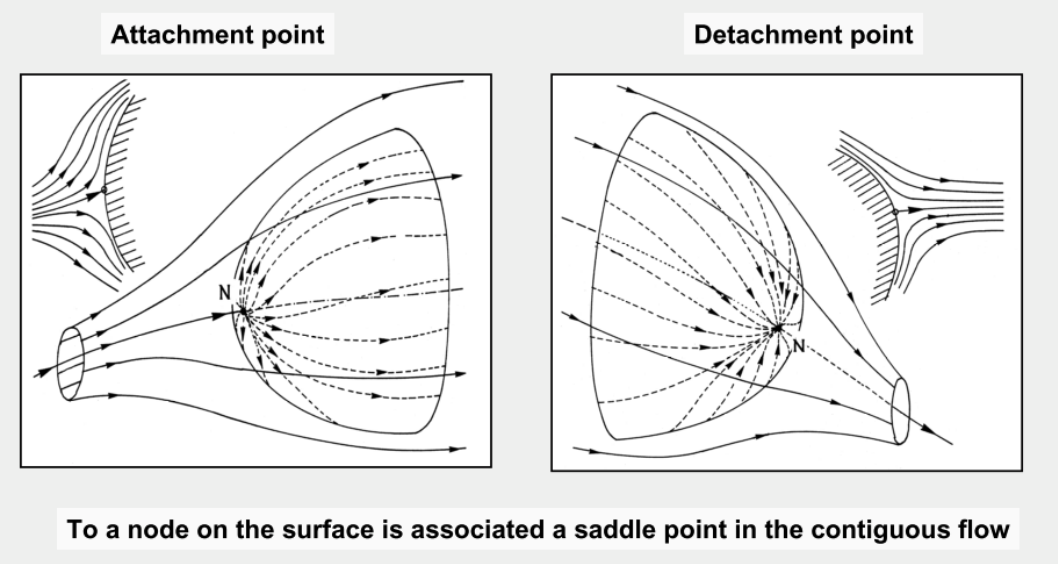

Figure 2.7: Surface flow topologies connect to the velocity field, from Delery et al. (2001).

the vicinity of the critical point can determine the local topology and that the local skin friction lines are correlated to the wall vorticity, the aim is to use knowledge of the vorticity map at 'primary separations' (those originating from flow features we can reliably predict will anchor separations) and use that knowledge to predict how the flow field will react to the downstream convection of vorticity bound by the separated front.

The idea of the SFSC is to unify our physical intuition about both of these processes to understand the complex flow field picture produced in strong corner interactions as in Fig.2.8. Despite the dramatic sidewall interaction in this figure, the Schlieren images were unremarkable, appearing nominally two-dimensional.

The primary challenge in applying CPT to an inlet flow is the odd behavior in the corner. Due to the orthogonal joining of the corner, and the velocity going to zero at both walls, the wall shear stress must also go to zero along the corner as well. However, because the flow along the corner is not 'separated' this effect of the

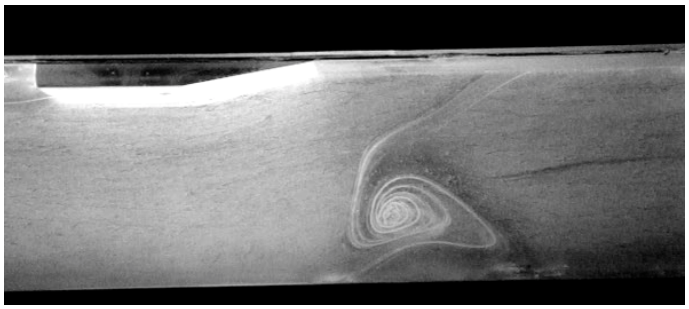

Figure 2.8: Strong sidewall vortex upstream of impinging shock from a previous study Eagle et al. (2011) visualized by oil flow following lines of constant (averaged) local skin friction. Flow right to left.

corner is such that any perturbation cause separation to occur from the corner region. Thus in Fig. 2.9, the corner of the interaction is created by creasing the paper. The primary separation, marked 'P,' occurs along the corner, and the foci, 'N', forms along the sidewall (imagine this by folding the paper ninety-degrees). However, this primary separation was caused by the upstream influence of the impinging shock! This is the crux of the SFSC. Primary perturbations to the flow field drive secondary structures which should they combine, form secondary structures in the flow. In this case, their are two primary sources, the wedge and the corner. There is a secondary interaction which occurs in the corner, and due to the narrow aspect ratio a secondary interaction also occurs along the centerline. First I will use the SFSC to examine and explain the sidewall/corner flow, and then I will address the centerline.

Returning now to the schematics of Fig. 2.4, we note that two-dimensional descriptions of the primary flow are only valid for such 'special' locations like the flow centerline, and we are left wanting for a 'convincing' description of the flow behavior in the presence of perturbations like sidewalls. Applying some simple intuition to the behavior of flow shear stress lines, we examine the hypothesis for symmetrical flow separation in three dimensions. A downstream blockage, like a post or injection, creates the horseshoe vortex pattern similar to the primary type separation, from

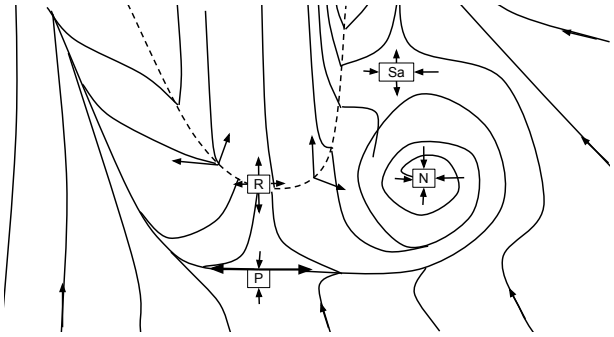

Figure 2.9: One possible pattern of a cross flow induced nodal separation. P - primary separation saddle point. R - reattachment node. N - separation focus. Sa - saddle point attachment

Fig. 2.3(a). However the second type, as described does not make physical sense in an enclosed flow. A nodal point of separation can occur if it is caused by two sources of counter-rotating upstream vorticity combine towards a point of significant strengthening of the streamwise vorticity component.

This is the basic argument of the SFSC. It classifies separations into two types, primary and secondary, takes hold of our knowledge of CPT to predict the local flow behavior in the 3DI-SBLI. The assumption of SFSC is that the flow first separates (a global type) due to disturbances to the 'primary' flow where the primary flow is the bulk motion of the fluid. Then, downstream of these primary separations, topological features (local separations) and the vorticity associated with them are given the chance to interact to form new global separations. It is the downstream interaction of halves of horseshoe vortices from two primary separations which cause a separation of the type from Fig. 2.3(b).

The purpose of the secondary flow separation concept is to use information about the local flow topology - and specifically the local vorticity - to predict the development of these flow separation topologies. Thus, one of the goals of this thesis work is to produce such a map and use the PIV velocity fields presented in the following

chapters to verify this idea.

To explain, let's consider two examples illustrating this process.

2.3.1 Supersonic Separation

In the case of fin generated SBLI, the most common sense approach is to consider the shockwave phenomenon as a combination of a primary flow, the canonical two-dimensional behavior far from the wall and a secondary flow, the local wall vortex. The flow induced by the streamwise turning of vorticity is termed 'secondary flow' in the manner of Bradshaw (1987). In CPT, Tabak and Peake (1982) showed that separation is always the source of concentrated vorticity. Thus if CPT is a valid explanation of flow behavior, then we can predict the behavior at the intersection of two 'lines of separation' in terms of the secondary flow induced by the primary separation vortices!

Consider a supersonic duct with an thin obstruction of variable angle of attack that spans the channel. The wedge is placed sufficiently far from the top and bottom wall such that the near field behavior is isolated from the walls' influence. Then, as the angle of attack of the obstruction is increased, the flow will eventually separate as determined by Korkegi (1975) and produce a secondary flow structure (Lu, 1993). Using CPT, we attribute this to a primary separation forming at the junction of the wedge in the sidewall boundary layer and a saddle point and two 'lines of separation' form. The lines of separation follow the foot of the swept shock that forms off the 'fin-plate' proceeds to convect towards the bottom wall of the wind tunnel. The origin of this secondary flow structure is the saddle point created by the wedge on the sidewall, and a horseshoe vortex (like in Fig. 2.3(a)) in this stagnation region is

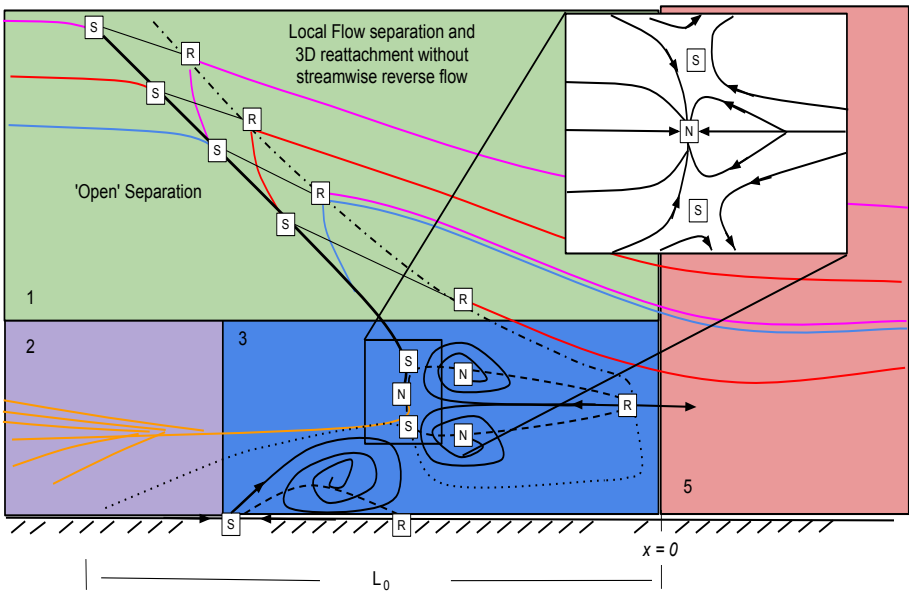

Figure 2.10: Sidewall skin friction lines depict 'open' separation and several sidewall interactions.

maintained under the shock foot both above and below the wedge.

If the interaction with the corner is sufficient to separate the flow in the corner (for corner flow separation requirements see Mojola (1976)) then this produces the first bifurcation of the flow field and the local line of separation splits into a focus of separation and a saddle point as shown in Fig. 2.9. A form of global separation has occurred in the corner, and a line of local separation forms from the saddle point created in the corner. Given the symmetry of the channel, similar behavior is occurring on the opposite wall. A whole series of interactions are possible depending on the strength of the vortices, their penetration towards the centerline, and the aspect ratio of the wind tunnel. Figure 2.10 shows a hypothetical SFSC weak corner separation on the sidewall. Figure 2.11(a) gives a picture of the bottom wall structure while Fig. 2.11(b) shows an end on view. The influence of the sidewall vortex slightly weakens the impinging shock, producing regions of attached flow near the sidewalls. However, the centerline separation is largely unchanged.

This is comforting perhaps, since we are accustomed to thinking of these problems as interactions between primary flows with negligible secondary (possibly turbulent) components. Such an argument is often put forward because the magnitude of such secondary flow patterns is but a small fraction of the overall mass flow. However, as outlined by CPT, these secondary flows are often attributable to a vortex driving/driven by a local type of flow separation. Thus the vortex is maintained by the line of separation until it reaches the opposite corner. To understand this vortex interaction, we employ the SFSC.

To define a topological profile in the case of asymmetric upstream conditions, consider a strong cross flow superposed on a primary separation (see Fig. 2.12). This was exactly the type of separation which occurred in the sidewall interaction in Fig. 2.8. However, for a strong corner interaction, as in our case, the potential for a new non-intuitive centerline topology emerges. Owing to the fact that the side wall structures of the swept shock interaction push further upstream of the local inviscid shock location, the corner flow separations will potentially occur significantly further upstream than the two-dimensional shock impingement location. This topology change is shown in Fig. 2.13

2.3.2 Two-Dimensional Separation

For a second example, imagine an infinite flat plate with some instability in the incoming boundary layer where low-speed 'streaks' approach a region of separation. Due to the nature of the secondary vortex flows known to develop such patterns, a new topology of primary separations followed by secondary separations is schematically represented in Fig 2.14 (Elsinga et al., 2010). In this case, secondary separations

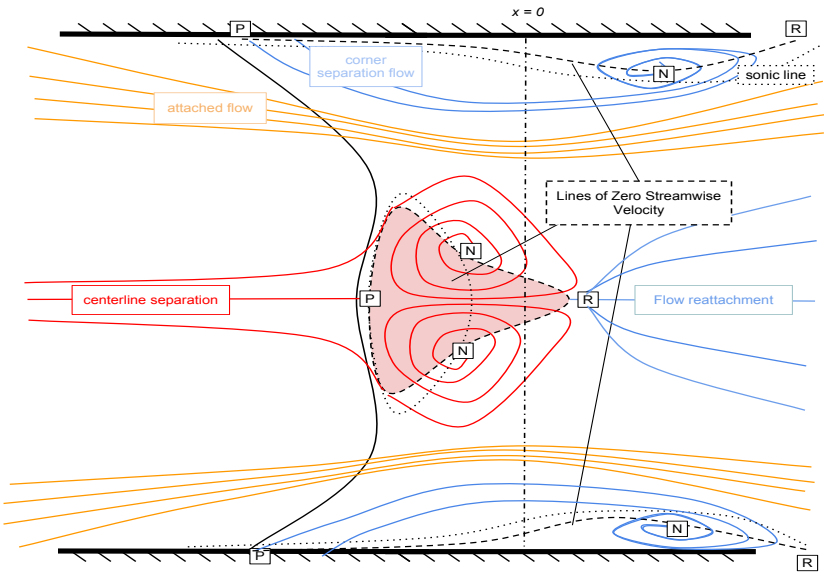

(a) Top View

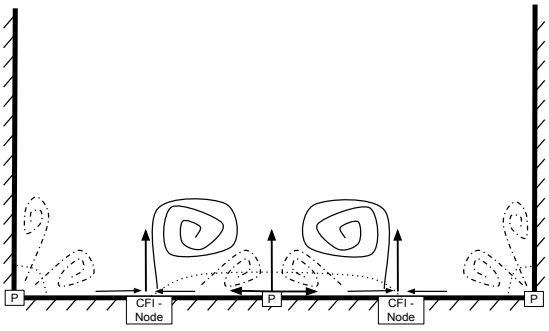

(b) Front View

Figure 2.11: Flow topology for strong separation with weak corner influence

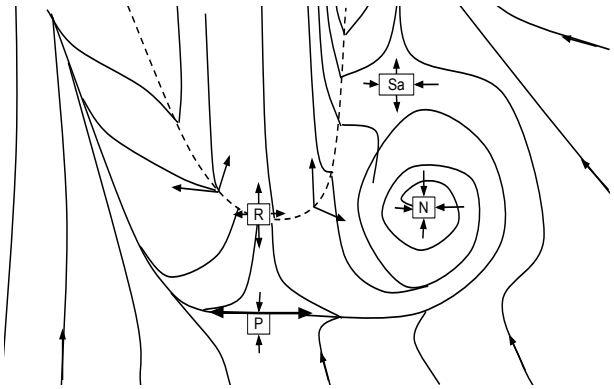

Figure 2.12: Primary separation in a cross flow develops a vortical instability. Primary flow from bottom to top, cross flow from right to left. Folding the paper along the centerline visualizes how a three-dimensional corner primary separation and a shock induced down-flow combine to produce the corner vortex pattern.

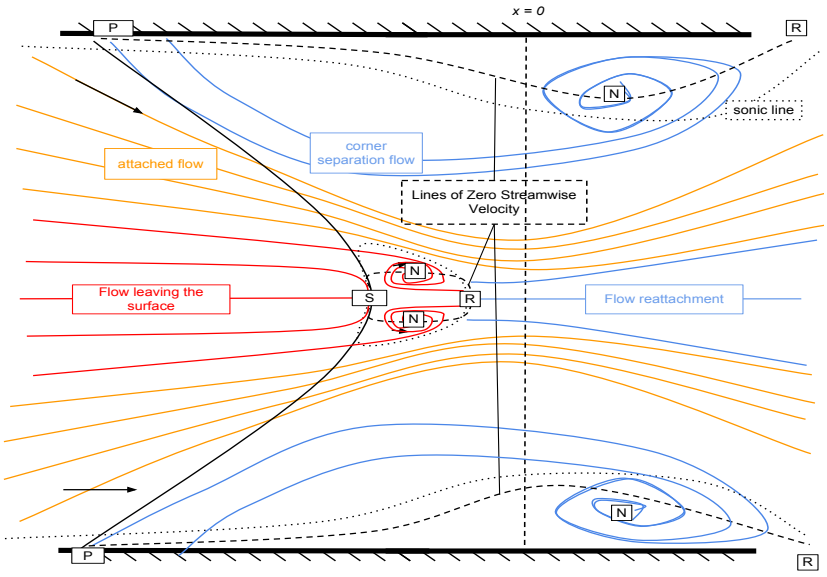

Figure 2.13: Flow topology along the bottom wall with a strong corner influence

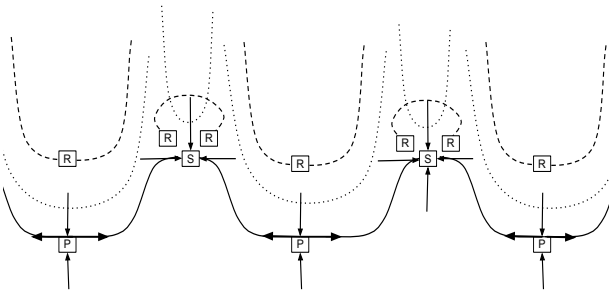

(a) Top View

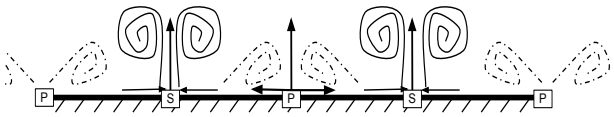

(b) Front View

Figure 2.14: Primary and secondary three-dimensional separation topology without sidewalls. Note that induced separations often occur downstream of two primary separations when these vortex structures merge and detach from the wall.

are driven by the cross flow induced by the upstream primary separations. This theory also explains the PIV results of Humble et al. (2009) in the separation region where crossflow is positively correlated with separation.

In Figure 2.14, the orientation of the vortex cores can be visualized in profile. We see that secondary separation is possible through the merging of two halves from a previous primary separation vortex and their subsequent detachment from the wall.

Due to unsteadiness in the turbulent boundary layer, the spacing of these separations will change in time. Thus, reflected shock motion for weak interactions is predictably driven by upstream influence in the boundary layer and the shock motion occurs on the order of the boundary layer thickness. However, stronger boundary layer forcing induces a boundary layer secondary flow structural response. It is therefore possible that passive boundary layer control strategies then impact this

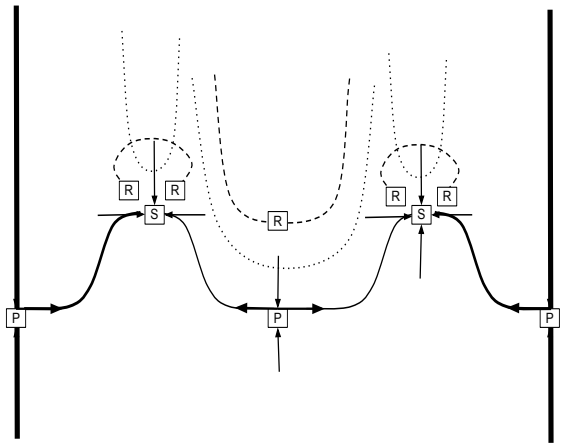

Figure 2.15: Sidewalls provide an anchor for primary separation to occur, and drive secondary flow away from the wall.

secondary flow structure by inducing a boundary layer secondary flow 'mode shape' ahead of the interaction.

Since a typical corner always has zero wall shear stress, it responds to perturbation by forming a primary separation (see Fig. 2.3(a)). The corner cannot be a secondary type unless flow along each sidewall is driven towards it (perhaps by suction). In nearly any SBLI the corner will act as a fixed point of primary separation. This constrains the boundary layer response to perturbations, and acts as a source of secondary flow away from the corners indicated by the bold lines in Fig. 2.10. Given that the action of both walls influences the momentum loss in the corner, we anticipate that the sidewall separates sooner than the main flow. Thus these primary separations will occur slightly upstream of the primary separation in the centerline of the flow.

2.3.3 Requirements for Verification and Potential Limitations

Perry and Chong (1987) describe an analysis of these critical points via the local

flow velocity but this has never before been verified with PIV. To confirm the SFSC hypothesis, this thesis must show that oil flow shear stress lines converge towards critical points identified by zero mean flow vorticity flanked by significant vorticity of opposite signs. Primary separation will be identified as a region of vorticity very close to the surface, while secondary separation will be indicated by vorticity further from the surface.

However, Tabak and Peake (1982) warns that, at any point in the flow where three-dimensionality is present, cautions should be taken when interpreting the flow field. Conclusions cannot be deduced from streamlines measured in a single plane. Only for 'special' locations, such as along a plane of symmetry, will such streamlines be identifiable actual paths traveled by a particle. For instance, streamline figures from spanwise planes showing circular paths. No fluid actually travels that path due to significant motion through the viewing plane. Instead, these measurements should be taken as representative of the averaged strain field. In this way, any streamlines are indications of the location and organization of background vortex patterns.

The biggest potential limitation to the method requiring a connection between the flow field and the skin friction is the unknown contribution from compressibility in the interaction. However, the secondary flows are well below the compressible limit ($M < 0.3$). Thus, we apply the secondary flow separation concept without addressing the effects of compressibility of the primary flow when describing flow interactions. For this purpose, it is sufficient to consider the shock wave solely as a source of vorticity in the boundary layer rather than of compressibility.

CHAPTER III

Experimental Facilities

Many details of the atmospheric in-draft supersonic wind tunnel facility that was used to generate and study the 3DI-SBLI was previously reported by Lapsa (2009). The pressure difference which drives this flow is provided by a remotely located low-pressure reservoir and can be maintained for five minutes. Non-intrusive optical diagnosis of the SBLI region, by means of stereo particle image velocimetry (SPIV), provides instantaneous and mean velocity data containing all three components of velocity. In addition, oil flow images, pitot and static pressure measurements, and Schlieren images were recorded to complement the PIV data. The present study is directed at illuminating the dominant three dimensional contributions occurring in internal flows with shock–boundary layer interactions (SBLI).

Previously, this 'Glass Inlet' wind tunnel has been used to study 2D-SBLI. Major details of the Stereo-PIV acquisition system remain consistent with Lapsa (2009). Thus, only a brief outline is presented. Several significant improvements in methodology to align this study with pertinent CFD validation efforts are also described. These include pressure, temperature measurements during each run, a correction to the laser triggering and camera timing and a new post-processing method. All of these procedures were adopted to facilitate future uncertainty studies. The last sec-

tion describes some of the features of the PIV algorithm which was used to generate the data visualizations in Appendices B-D.

3.1 SBLI Geometry in the Michigan "Glass Inlet"

Fig. 3.1 shows a schematic of the experimental arrangement. Supersonic flow at a fixed design Mach number of 2.75 is produced by a one-sided converging-diverging nozzle. Velocity data are collected in two dimensional planes oriented in streamwise vertical, streamwise horizontal, and spanwise vertical directions. Data in spanwise planes located in two locations upstream of the shock generator provide inlet boundary conditions to support modeling efforts and to understand the secondary flow development upstream of the interaction. High-resolution velocity data throughout the interaction region provide high-fidelity information about the interaction region. One transverse plane downstream of the interaction provides assessment of inlet 'distortion' (i.e. non-uniformity due to boundary layer and shock effects) through the interaction. A close up visualization of the data locations is given along with the data in §5.1, §5.2, and §6.2. In tunnel coordinates, the x-coordinate is aligned with the streamwise direction, the y-coordinate is aligned with the wall-normal direction, and the z-coordinate is aligned with the spanwise direction and $x = 0$ is defined as the start of the 'inlet' at the leading edge of the shock generator. The nozzle and test section, including shock generator geometry, can be reconstructed for modeling or experimental purposes by using the dimensions given in Appendix A.

Figures 3.2, 3.3 and 3.4 provide pictures of the laboratory setup including the installed wedge, cameras and laser optics. The vacuum-driven, or "suck down" wind tunnel facility is unchanged from previous investigations (Lapsa, 2009). The constituent modular sections include a bell mouth, flow conditioner, subsonic converging

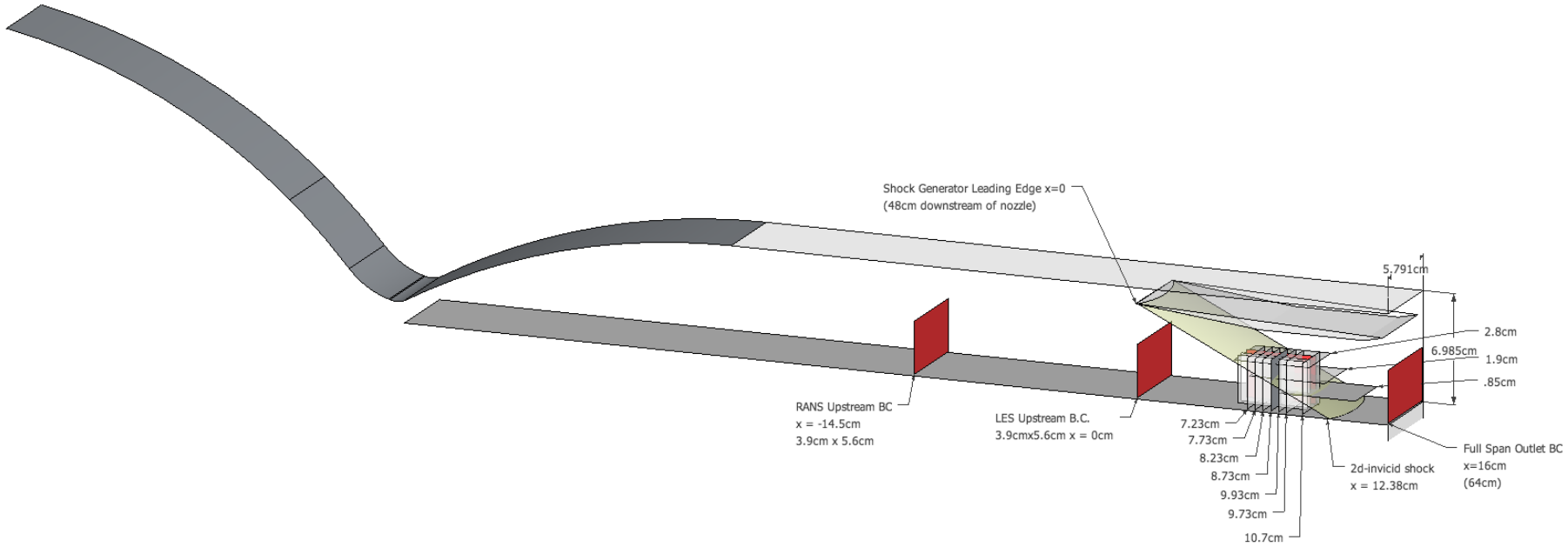

Figure 3.1: Data Locations within the Michigan Glass Inlet. *x=0 mm* coincides with the shock generator leading edge. Inviscid shock impingement occurs around *x=120 mm*. Note: Actual viscous shock intersection occurs near *x=90 mm* and upstream influence reaches to *x=80 mm*

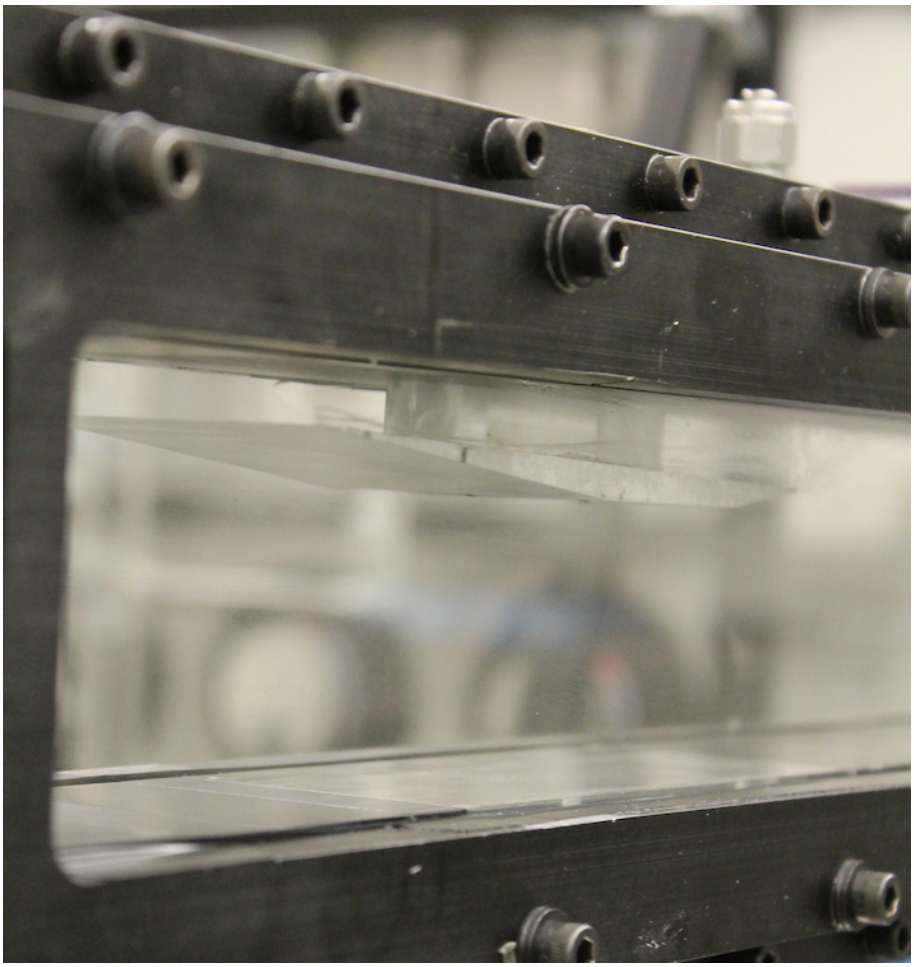

Figure 3.2: Close up of suspended 6° wedge installed in tunnel. Flow left to right.

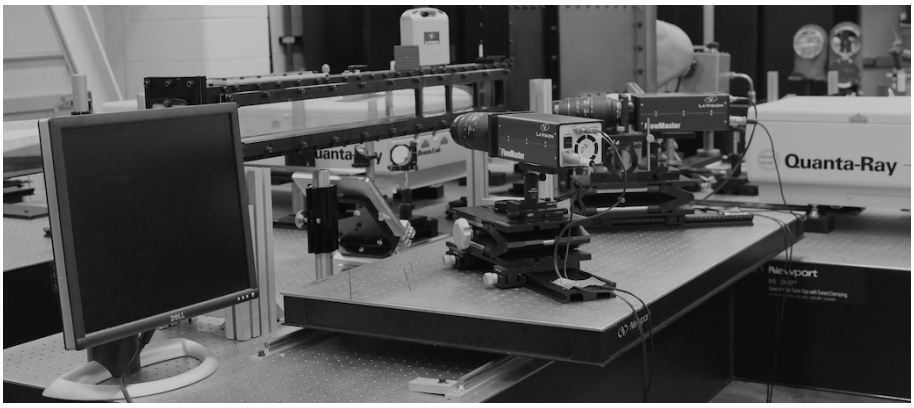

Figure 3.3: Camera setup oriented at 33° for spanwise imaging. Flow from right to left.

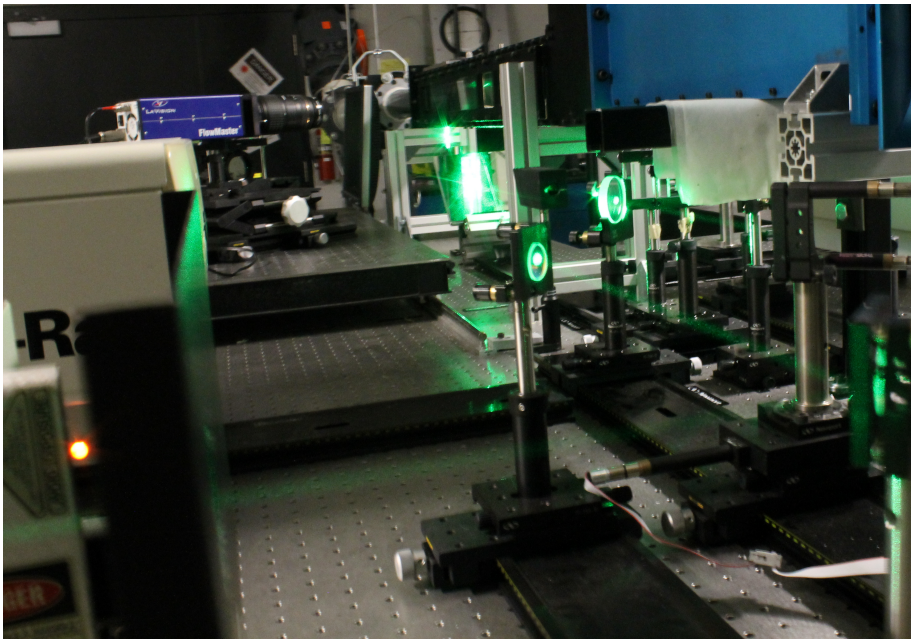

Figure 3.4: Laser Optics

nozzle, supersonic diverging nozzle, test section and diffuser.

The test section is a rectangular constant-area duct of dimensions$57.2 \times 69.9\, mm^2$. A strut holds the full span wedge assembly used to produce an oblique shock wave that propagates along the sidewalls and across the tunnel until it interacts with the bottom-wall boundary layer. The strut and wedge assembly is installed along the top wall of the test section, and is shown in Fig. 3.2. The leading edge of the strut is located 861mm downstream of the nozzle entrance. This downstream location was chosen by Lapsa (2009) to balance several competing requirements: 1) the bottom wall boundary layer is sufficiently large (1cm) so that the velocity profile can be resolved using the SPIV technique and 2) a zero-pressure gradient profile is approached while 3) limiting the boundary layer Reynolds numbers,$Re_{\delta^*} < 20,000$, $Re_\theta < 10,000$ (full detail in Table 6.2) in order to accommodate computational efforts.

A 6° full span shock generator is fixed to the strut for this study. The leading

edge provides a convenient origin from which other relevant dimensions are defined. For a nominally 2-D flow, the pressure ratio across the shock system is predicted to be $p_3/p_1 = 2.73$ for $M = 2.75$ based on incoming free stream conditions. The oblique shock wave propagates across the test section and impinges on the boundary layer formed along all three walls of the test section, producing the interactions that are the topic of this study.

Upstream of the interaction, the lower wall boundary layer height is $\delta_0 = 8.5\,\mathrm{mm}$, as measured in §6.2. The strut fixes the wedge 9.2 mm from the test section top wall and thus it resides sufficiently outside of the top-wall boundary layer to ensures a steady shock whose anchor point does not fluctuate due to turbulence present within the top-wall boundary layer.

Optical access is provided along the entirety of the test section by windows that form the side walls. These allow the PIV cameras to image the interaction region while being arranged in their stereo positions. They also provide access for the laser sheets to enter the test section in the direction normal to the free stream velocity and thus they illuminate spanwise-oriented planes. An additional window is mounted flush along the lower boundary to enable imaging of the streamwise (both horizontal and vertical) planes.

3.2 Measurements

3.2.1 Oil Flow

Oil flows are a well established method for determining flow separation and the flow topology along limiting surface streamlines, including separation zones. In this study, the oil mixture is created by mixing kerosene and calcium carbonate powder

in ratios five parts to two, by volume. Prior to tunnel operation, a three-inch silicone brush is used to apply the combination to the walls of the wind tunnel perpendicular to the expected direction of flow. Once the valve is opened to start the tunnel, viscous forces, $[\tau_x \ \tau_z]$, drag the solution along the wall in trajectories of local skin friction. Because kerosene is highly volatile, the low-pressure operating condition at Mach 2.75 evaporates the kerosene, affixing the calcium carbonate to the walls in the pattern of skin friction lines. The mixture accumulates in regions of skin friction convergence along lines of separation and at separation nodes and foci and does not evaporate as readily. Lu (2010) describes a method for characterizing the behavior of these lines in a swept shock. Variations in skin friction line convergence indicate the relative strength of this swept shock boundary layer interaction along the sidewall. Photographs are taken of the developing oil flow patterns using a Sony DSC-t70 8.2 Megapixel camera at 720×640 pixel resolution, and 30fps video with a Sony HDR-SR12 at 1920×1080 pixel resolution. The videos document the startup transients, the unsteady motion in the recirculation zones, and the relative magnitude of the flow field three dimensionality. Still images, as well as individual frames from the video, are used to characterize the topological development of these flows and to ensure repeatability.

3.2.2 Schlieren and Shadowgraph

Images gathered from a Schlieren system were used to verify the repeatability of the flow field during oil flow studies of different geometries (Eagle et al., 2011). A CCD camera was employed to digitize the images at a 1280×1024 pixel resolution. The light source was an Oriel Labs 100 watt mercury lamp. Image exposures

were feasible down to $25\mu s$ resolution but these images had a dynamic contrast of 2. Instead images were exposed for $100\mu s$, and achieved dynamic contrast of 10. Unfortunately, this light source is not powerful enough to allow image exposures short enough to resolve features in the boundary layer. At the leading edge of the shock generator, flow deflection angles were measured from the Schlieren images and checked against estimated values based on the Mach number and the $\theta - \beta - M$ relations in §4.1

3.2.3 Stereoscopic Particle Image Velocimetry

Except in the case of the spanwise imaging planes, where the out-of-plane velocity component is approximately 600 m/s, the methodology used here is unremarkable compared to typical SPIV measurements. The special treatment required in the spanwise planes, as well as other elements essential to the technique such as the light sheet generation, seed particles, seed density, and particle imaging, will be outlined.

Stereoscopic particle image velocimetry (SPIV) produces a single-color cross-correlation PIV measurement. Two interline transfer CCD cameras with 1280×1024 pixel resolution and two Nd:YAG lasers are coordinated by a computer with an onboard programmable timing unit. Each individual particle image is a single-color, double-frame, single-exposure PIV image acquired at an angle normal to the light-sheet, thus allowing two cameras oriented in a stereo configuration to determine the two in-plane velocity components and the one out-of-plane velocity component over the measurement field-of-view. The 532 nm light sheets formed by the Nd:YAG lasers illuminate the particles.

3.2.3.1 Light Sheet Generation

To illuminate the seed particles in the field-of-view, a pair of light sheets are created using two frequency-doubled Nd:YAG lasers (one Spectra-Physics Quanta-Ray Pro-250 and one Spectra-Physics GCR-3). The lasers are sequentially triggered to create the double pulse of the 532 nm sheets, each with total energy of approximately 200 mJ. The flashlamps and Q-switches are triggered by TTL signals at 10 Hz with a pulse duration of 10 ns. The interframe time, Δt, between pulses is controlled by a PC-based programmable timing unit (PTU) controlled by the LaVision DaVis 7.2 PIV acquisition software.

Both lasers have a 100 ns intrinsic delay between the rising edge of the trigger pulse and the actual peak in laser energy. This additional delay is significant for the flow conditions used in the present study, and causes the actual interframe time Δt, determined by the peak-to-peak in laser energy, to differ from the target interframe time Δt_0, determined by the trigger pulses. Thus, quantification of Δt is performed before each data run. This is done using a ThorLabs DET10A/M high-speed photodetector connected to a LeCroy WaveRunner 6030 350 MHz oscilloscope. Realtime adjustment of the DaVis software allows the internal delay to compensate for additional equipment delay until the measured Δt is the same as commanded by the PTU.

The laser paths are identical to previous study (Lapsa, 2009) except for the addition of streamwise horizontal planes. In that case, the sheet forming optics are rotated 90° to produce a horizontal rather than vertical laser sheet. To limit out-of-plane particle loss from Frame 1 to Frame 2, the laser sheet thickness must be large in comparison to the out-of-plane particle displacement. In most typical applications, this requirement is automatically satisfied since the full-width at

half-maximum of a typical 532 nm Gaussian beam waist is approximately 250 nm. For the spanwise planes in the present work, however, the nominal flow direction is oriented normal to the laser sheet and thus the out-of-plane velocity component is approximately 600 m/s. Current state-of-the-practice camera hardware limits the inter-frame time to a minimum of approximately 500 ns, giving typical out-of-plane particle displacements of approximately 300 μm. The sheet thickness must therefore be made considerably thicker than the minimum Gaussian beam waist. Note, however, that an increasingly thick sheet introduces volumetric effects not accounted for by two-camera SPIV algorithms. Thus, a tacit optimization process, in which the sheet thickness is adjusted in conjunction with the camera aperture, camera angle, Scheimpflug angle, laser intensity and other aspects of the arrangement, takes place in order to minimize both particle loss and volumetric effects. Given an estimate of the sheet thickness, Adrian and Westerweel (2010) recommends a particle displacement less than 1/4 the sheet to minimize particle dropout. Table 3.2 gives the sheet thicknesses, Δl, used in each image plane.

3.2.3.2 SPIV Seed

To seed the flow in this study, an oil aerosol is generated using a TDA-4B portable Laskin nozzle aerosol generator from ATI Techniques. The generator consists of an array of six Laskin nozzles that create polydispersed sub-micron particles. Using a Poly-Alpha Olefin (PAO) oil with density 819 kg/m^3, also provided by ATI Techniques, the mean particle diameter created by the generator is specified to be 0.281μm. Three valves enable any number of the nozzles to be operated simultaneously, thereby allowing for a wide range of aerosol concentrations. However, dense

seeding concentrations quickly foul the measurement when oil particles deposited in regions of the flow and illuminated by the laser produce glare in the images, thus only a fraction of the first valve (2/3 open) was actuated to seed the entire flow in this study.

Inherent in any PIV measurement within confined duct flows is the propensity for the seed particles to accumulate on the walls and windows of the duct. This well-known issue is not merely an annoyance; it results in limited run times and thus limits sample sizes. Data sets of 1700 images require 17 tunnel runs acquiring 100 images per run. Downtime to clean windows between runs requires approximately 15 minutes. Thus each data plane is completed in one or two days.

PIV seed particles can also be characterized by their particle Stokes number. This is defined as:

$$St \equiv \frac{\tau_p}{\tau_f}, \tag{3.1}$$

where τ_p and τ_f are the characteristic particle and flow time scales, respectively. The characteristic particle time scale is derived from Stokes law for spherical particles to be

$$\tau_p = \frac{\rho_p d_p^2}{18\mu}, \tag{3.2}$$

where ρ_p and d_p are the particle mass density and mean diameter and μ is the dynamic viscosity of the surrounding fluid. The characteristic flow time scale for a turbulent shear flow is defined from the local outer length scale $\delta(x)$, in this case the local full width of the boundary layer, and the local outer velocity scale, U_∞, in this case the local free stream velocity, so that

$$\tau_f = \frac{\delta(x)}{u_\infty}. \tag{3.3}$$

Clemens and Mungal (1991) have shown that particle slip is negligible if the particle

Stokes number $St < 0.5$ for typical incompressible flows. Samimy and Lele (1991) showed computationally that in compressible flows, $St < 0.25$ particles could adequately track the large scale motions but that for $St > 0.05$ they were not capable of tracking the smallest scales. Urban and Mungal (1998) showed experimentally that particle slip is negligible if the Stokes number $St < 0.1$ in supersonic flows.

In this study, an oil aerosol is generated with a mean particle diameter specified by the manufacturer of $0.28\,\mu$m. The particle relaxation time is $\tau_p \approx 0.44\,\mu$s. For the $M = 2.75$ free stream, the characteristic flow time scale is $\tau_f \approx 17\,\mu$s thus the particle Stokes number is $St \approx 0.026$. This readily meets the criterion noted above. The particle size was independently verified by assessing the relaxation distance as the particle passes through a shock (Lapsa, 2009). This result suggests that the polydisperse nature of the particles are closer to $0.44\,\mu$m and thus the measured particle stokes number is still within the acceptable range ≈ 0.1.

The particle images are recorded by two SensiCam PCO interline transfer CCD cameras at 3.33Hz (limited by the camera DRAM aquisition). The CCD has a 1024×1280 ($h \times w$) pixel array and a physical chip size of $6.8 \times 8.6\,\text{mm}^2$. The 12-bit signal depth provides sufficient signal dynamic range, and electronic Peltier cooling ensures low noise.

Each camera is equipped with a Sigma 70-300 f /4-5.6 APO macro lens to allow up to 1:1 imaging at a minimum focal length of 40.1 cm. For each camera, particle images from the first laser pulse are recorded onto the first frame and then immediately shifted under the submask. The particle images from the second laser pulse are then stored on the second frame after the time separation Δt.

Previous use suggested that reliable camera operation ceased for $\Delta t \lesssim 800\,\text{ns}$. Below this level, the pixels near the horizontally outer boundaries were unsuccessfully

transferred under the submask resulting in low or zero signal levels at those locations. However, this limitation was removed by advancing the 'signal delay' sent to the cameras to initiate the beam straddling. As in the previous study, the spanwise planes require interframe times below 550 ns, however now the full CCD 1024×1280 can be used where previously, only the central third of the CCD was available for imaging. To keep consistent parameters for uncertainty studies the illumination and timing of the streamwise planes was kept constant.

The two cameras are arranged differently for imaging of streamwise and spanwise planes. Imaging of spanwise planes is done using the forward/forward camera configuration, in which both cameras image the particles in forward scattering mode. For imaging of the streamwise planes, the laser sheet enters the test section perpendicular to the camera and as a result both cameras image the particles in side-scattering mode.

The small field-of-view of the measurements, coupled with the long focal length of the camera lens, dictates that a small aperture setting together with the Scheimpflug criterion must be used to create particle images that are focused across the full extent of the field-of-view. The small aperture has the additional advantage of reducing image aberrations such as coma and astigmatism. In the present work all images were captured using an aperture setting f/#11 except in the horizontal plane, where f/# of 4 was used to provide a more limited depth of field to avoid visualizing streaks in the bottom wall as particle data.

Image Plane	$f/\#$	$l_x[mm]$	$l_y[mm]$	$l_z[mm]$	η $[\mu m/pix]$	$DSR_{max} = \frac{l_{max}}{\eta * X_{pmax}}$
Trvs BC's	11	–	37.5	54.3	37.5 ± 1.0	113
Transverse	11	–	25.9	34.4	26.5 ± 0.5	101
Strm Vert	11	50.6	28.0	–	37.0 ± 0.5	106
Strm Horz	4	44.0	–	32.3	39.5 ± 1.5	87

Table 3.1: Camera Settings and Dynamic Spatial Resolution

Image Plane	$\Delta l[mm]$	dt	$DVR_x = \frac{u_{max}}{\sigma_u}$	$DVR_y = \frac{v_{max}}{\sigma_v}$	$DVRz = \frac{w_{max}}{\sigma_w}$
Trvs Full Span	1.25±0.25	600 ±10	$\frac{597}{14} = 43$	$\frac{\pm 80}{7} = 11$	$\frac{\pm 80}{7} = 11$
Transverse	1.25±0.25	600 ±10	$\frac{597}{14} = 43$	$\frac{\pm 80}{6} = 13$	$\frac{\pm 80}{6} = 13$
Strm Vert	1.0±0.25	600 ±10	$\frac{597}{7} = 85$	$\frac{\pm 80}{7} = 11$	$\frac{\pm 80}{14} = 6$
Strm Horz	1.25 ±0.25	600 ±10	$\frac{597}{8} = 74$	$\frac{\pm 80}{15} = 5$	$\frac{\pm 80}{8} = 10$

Table 3.2: Laser Settings and Dynamic Velocity Resolution

3.2.3.3 Post-Processing

The LaVision DaVis 7.2 software package is used to compute the spatial cross correlation and resulting velocity components using a multi-pass algorithm with interrogation boxes decreasing from 32×32 pixels to 16×16 pixels and 50% overlap. Consistent Δt and relative sizes of the different field of views ensure that consistent interrogation window sizes are appropriate. Tables 3.1 and 3.2 report relevant processing parameters for the cameras and lasers. Table 3.3 estimates the number of measurements possible in one boundary layer thickness for each plane.

Image Plane	$\delta_0/IW(50\%)$
Trvs BC's	$\frac{8.5}{0.038 \times 8} = 28$
Transverse	$\frac{8.5}{0.027 \times 8} = 39$
Strm Vert	$\frac{8.5}{0.037 \times 8} = 29$
Strm Horz	$\frac{8.5}{0.039 \times 8} = 27$
Lapsa(2009)	$\frac{10}{0.025 \times 16} = 42$

Table 3.3: Estimated number of measurements within the boundary layer by image plane.

An academic research code was used for additional post-processing and data handling in the Matlab computing environment. The software, PiVMat, was written by Frederic Mosey for 2D PIV studies. Data handling is accomplished in a 'struct' variable which stores x-y locations, and velocities, as well as documents and records all data processing. Functions are coded to calculate average, gradient, and fluctuating quantities. Uncertainty quantification based on the number of valid vectors can also be determined. The code has been substantially modified to operate on three dimensional vector fields.

3.3 Uncertainty

A number of features contribute to the uncertainty of PIV measurements. An exhaustive list was compiled at the PIV Uncertainty workshop held in Las Vegas in March 2011. The methods adopted here to address, estimate or reduce both systematic (i.e. epistemic/bias) and random (i.e. aleatory/stochastic) uncertainties are described below. Work to report uncertainty bounds from the data is ongoing.

3.3.1 Run Condition Monitoring

Ambient air pressure and temperature was recorded for each run from a hallway barometer and a thermocouple located in the room. Static pressure in the test section was visually monitored by analog Omega vacuum gauges(PGC-20L-30V/30 -30inHg $\pm 3\%$) at three places along the length of the test section. Downstream static pressure at the valve was recorded at the beginning and end of each run as a measure of the variability of the back pressure on operating conditions. In tandem,

a shadowgraph system was employed to visually assess repeatability in the shock location and relative steadiness of the shock over the 90 second test time. Run times of greater than 6 minutes were required to view transient behavior due to the back pressure at the shock impingement location, thus the measurements in the SBLI location are determined to be independent of the back pressure.

3.3.2 PIV

Uncertainty in PIV is related to the local RMS of the measurement, which is clearly affected by turbulence, as well as flow gradients, but all of these are impacted by the number of valid measurements taken at each location. A novel technique for vector validation is possible using the PiVMat code. Rather than using a local median filter in each image, vectors can be compared to the ensemble result for each point in the plane. The PiVMat code was updated to track the number of valid measurements at each interrogation window so that a map of 'uncertainty' could be developed. This is useful when irregular seeding prevents some regions from recovering a high percentage of valid vectors. For most images this uncertainty map ranges between 95-99% in the core flow to 30-50% in low momentum regions.

Global reference points were difficult to track to ensure that consistent coordinate systems are possible for direct measurement comparison from plane to plane. Stereo-PIV self calibration methods shift the effective center of the plane by up to $\pm 1/2\Delta l$. In addition, each measurement is a volume average quantity of the volume that happens to have particles. In regions containing shocks and large gradients the native fluctuation of the measurement is strongly influenced by this. Validation quality data for such intricate interactions requires higher fidelity methods of locating data planes to reduce uncertainty especially in high gradient regions. A 1 mm shift

in the streamwise location of the shock has a significant impact on verification efforts for computational fluid dynamics simulations. An effort was made to locate precisely where these measurements were taken, however improvements are needed to ensure this process is robust. Manufacturing of laboratory wind tunnels for such validation exercises do not currently have built in methods for such 'Global Positioning Systems.'

CHAPTER IV

Oil Flows, Schlieren and Pressure.

It was Korkegi (1975) who first helped determine the principle drivers of performance in multi-dimensional SBLI. He showed that the type of interaction is important for determining how sensitive an SBLI is to separation. His collected data is repeated in Fig. 4.1. This result emphasizes the need to understand drivers of the transition from two to three-dimensional separated flows. In this chapter, several traditional methods for investigating the nature of the UM 3DI-SBLI are used and compared to previous studies.

4.1 Schlieren and Shadow Graph Images

Data from Schlieren images produced the first pictures of SBLI separation (Gadd et al., 1954; Chapman et al., 1957). The techniques average across the flow field, and random spanwise variations in shock position result in essentially the same image from frame to frame. Thus, hardly any three-dimensional data can be acquired using this traditional technique. A sample shadowgraph image of the Michigan 3DI-SBLI at the bottom wall is presented in Fig. 4.2. All that is revealed by viewing several such images is a slight rippling in the reflected shock. The lack of motion in the impinging shock suggests that the incoming core flow is relatively steady. However, it is well

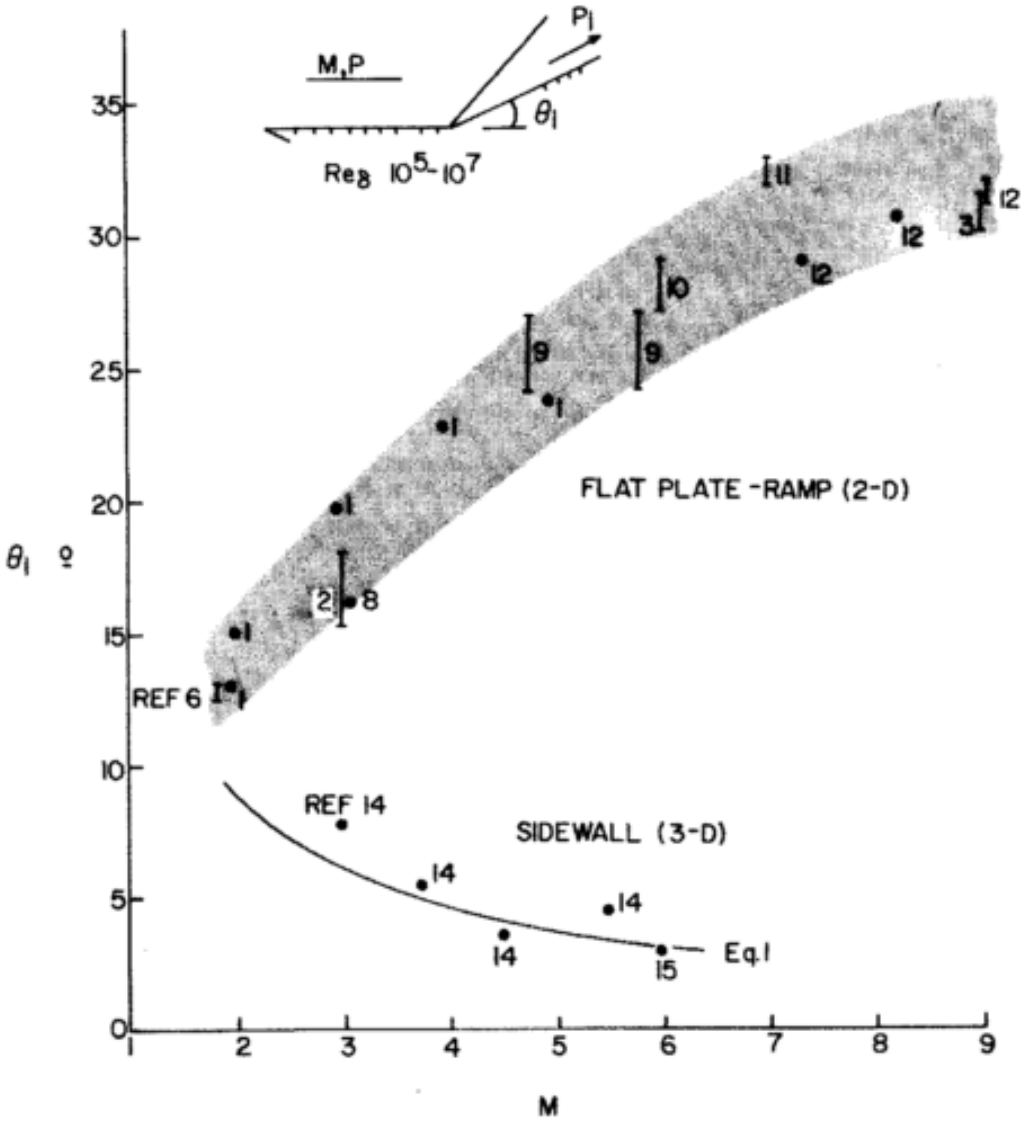

Figure 4.1: Effect of Mach number on the wedge angle which provokes separation in 2D vs. swept interactions from Korkegi (1975)

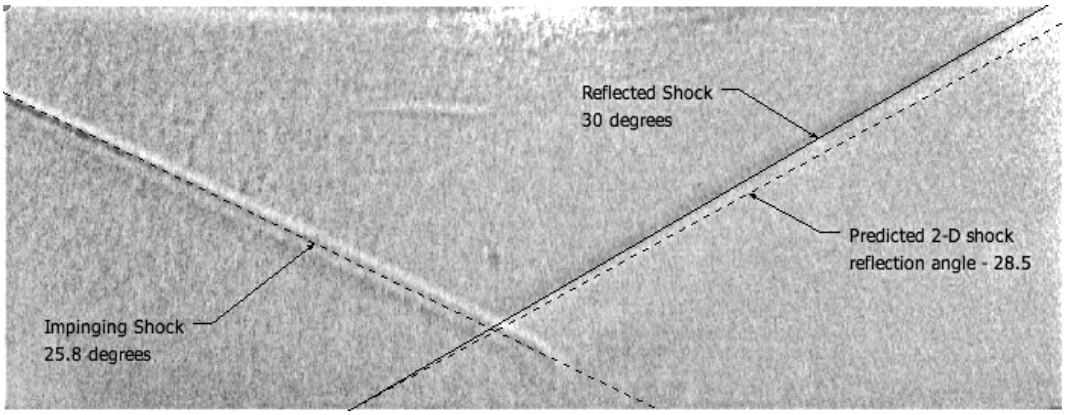

Figure 4.2: Shadowgraph of 3DI-SBLI appears largely two-dimensional. Only the apparent shock thickness indicates any three-dimensional behavior.

known that the free-interaction region in turbulent flows is actually characterized by a translating shock/compression system across which the instantaneous pressure rises abruptly, and this effect is only smoothed out in any time, space, or ensemble averaged data.

While the physics just described adequately deals with an undisturbed turbulent boundary layer reacting with a shockwave in the center of the tunnel, accounting for an inlet simulation also brings in the effect of the sidewall interference in the shock generation process. Studies relevant to such sidewall interactions are reviewed by Lu (1993) who finds that for a swept shock interaction, the controlling parameter is the Mach number incident normal to the swept shock wave, much as is the case with an oblique shock wave in a free stream flow. However, as discussed by Kubota and Stollery (1982), a system of wedge vortices are likely to form underneath the shock foot. Schematics of these interactions are reproduced in Fig. 4.3.

To better understand the three-dimensionality in this flow, oil flows were performed to compare with the Schlieren span average images. Figure 4.4 shows the relative location of oil flow to shock location for the case studied. All in all, the Schlieren data does not provide adequate information about the spatial gradients to

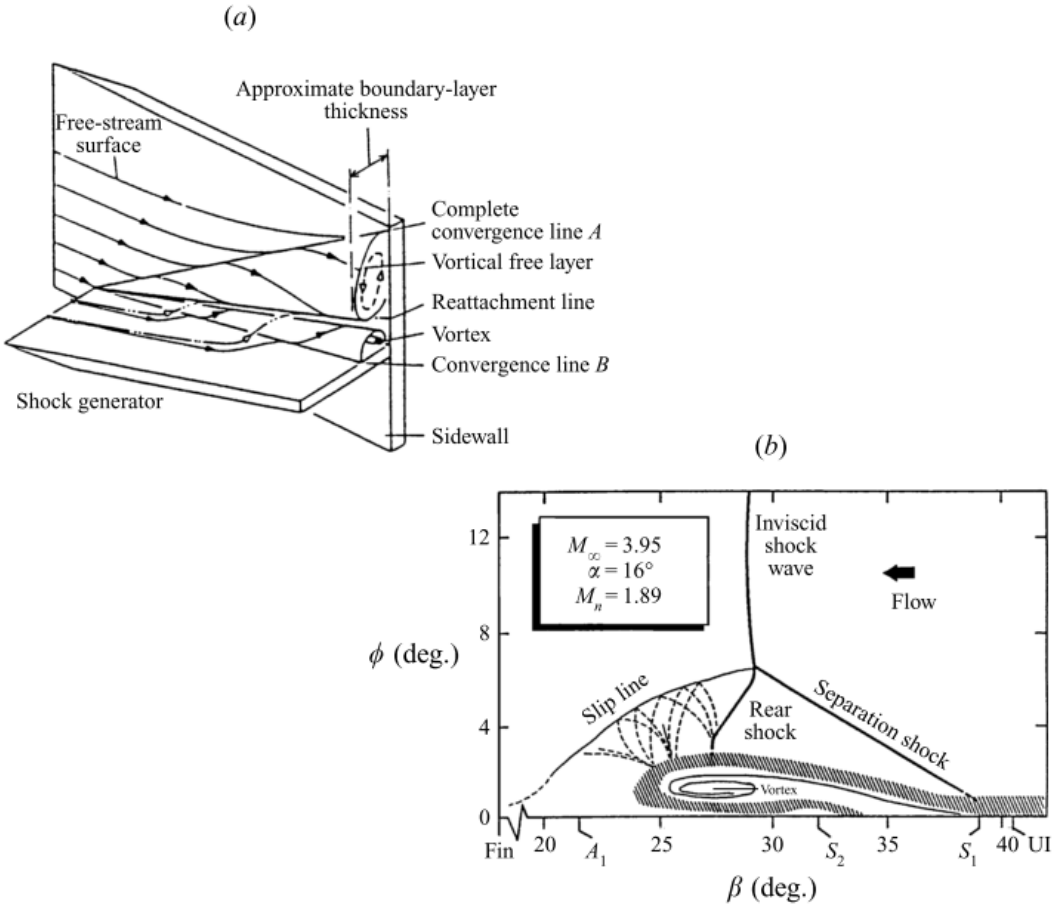

Figure 4.3: A model of swept fin interaction generated vorticity on oil flow lines proposed by Kubota and Stollery (1982). (a) Three-dimensional flow schematic. (b) Interaction structure along a plane normal to the inviscid shockwave

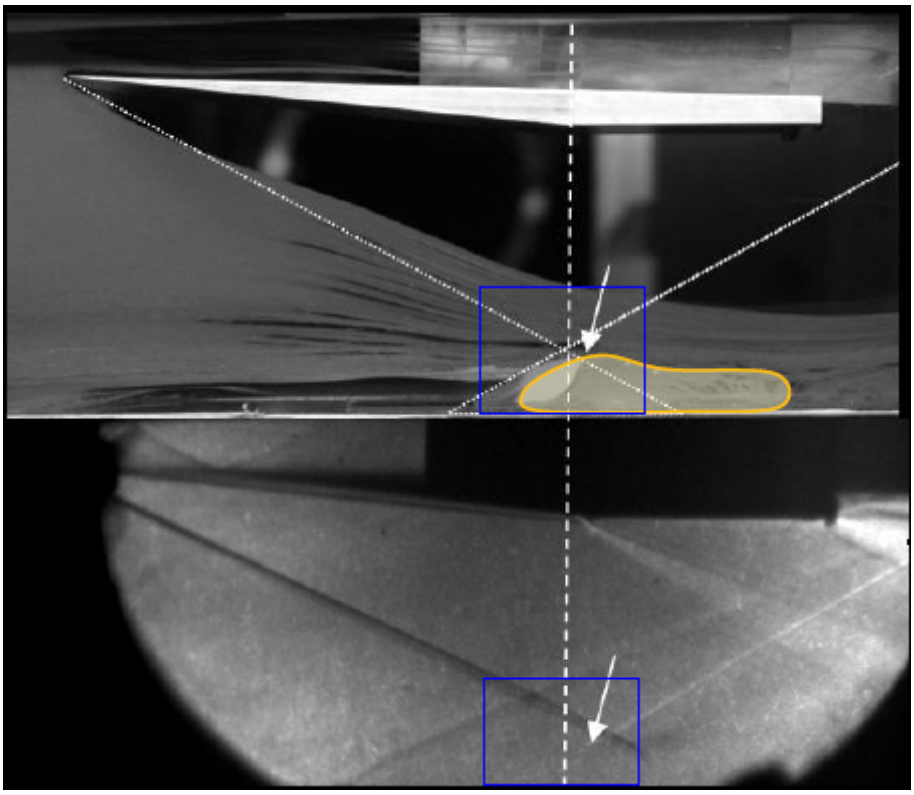

Figure 4.4: By comparison of oil flow and Schlieren photos we gather that interaction region is upstream of the 'span average' shock location.

make any definitive conclusions about the oil flow pictures, other than to indicate that the presence of the shock wave boundary layer interaction responsible for the development of these flow features. Further Schlieren images were used only for flow repeatability confirmation and oil flow was considered the primary means of determining three-dimensional behavior instead.

4.2 Bottom and Sidewall Oil Flows

Oil flow visualizations, on the other hand, are useful qualitative tools for understanding near wall flow three-dimensionality because thin oil films follow the local shear stress lines (Squire, 1961). Yet, as recently pointed out by Lu (2010), discrepancies between authors regarding 'separation' when the local shear stress converges

but doesn't go to zero in the interaction has led to uncertainty regarding the nature of three-dimensional separated flows due to the opposite trends in conditions required for two-dimensional 'incipient' separation compared to three-dimensional, or swept-type, interactions (Korkegi, 1975).

The secondary flow separation concept (SFSC) outlined in the previous section (§2.3) is evaluated in this example 3DI-SBLI using images of oil flow shear stress lines. SFSC predicts that 'global' changes in surface flow topology arise from interactions between vortical structures which induce and are induced by separation. Because the shape of the skin friction lines must be coupled to the local flow velocity, measurable changes in the flow topology must coincide with changes on the surface topology. However, to complete this picture requires extensive review of several phenomenon in the literature including fundamental understanding of normal shock boundary layer experiments, swept or 'fin-plate' shock boundary layer investigation and generalized secondary flow of Prandtl's second type (more commonly 'corner flow') to determine what the local vortical flow induced by each of these is individually.

Without the SFSC, the only hypothetical flow structures that are available to form 3DI-SBLI is an amalgamation of several of these other unit physics problems, including a normal shock, swept shock and corner flow. However, such a linear superposition is rarely possible in pure velocity space because any significant deviation from stable operating conditions rapidly break down the linear perturbation approach. Therefore, a new three-dimensional flow paradigm is sought which reformulates understanding from each of the canonical 2D problem archetypes into a three-dimensional secondary flow separation concept. Drawing on earlier topological methods, measurements for the first time differentiate which flow topology drives the surface flow.

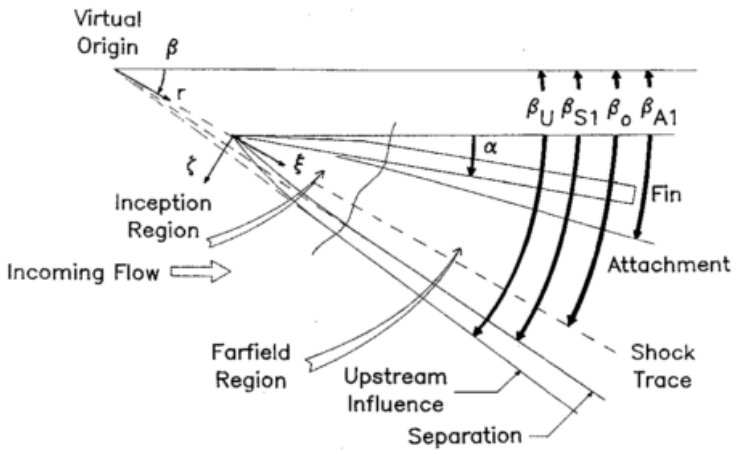

Figure 4.5: Key surface features of Fin-Plate Interaction

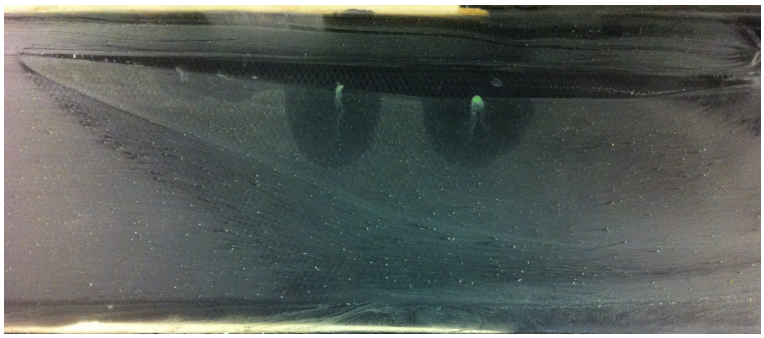

Figure 4.6: Sidewall oil flow through the interaction region

In this study, the sidewall interaction extends significantly upstream of the inviscid shock location as shown in Figs. 4.4 and 4.6. In Fig. 4.7 the bottom wall shows attached flow at the centerline. An explanation for these features is logically deduced from the start-up sequence of images in 4.8 and described below using the schematic of this upstream influence behavior discussed by Lu (1993). Relevant parameters and a sketch of the interaction are reproduced in Fig. 4.5. Theoretical aspects of such spanwise influence is discussed in the work of Inger (1987) suggesting how such behavior must translate away from the local interaction.

A time sequence of oil flow start up that helps us to understand this process is presented in Fig. 4.8. In particular, there is a rapid convergence of oil flow lines near

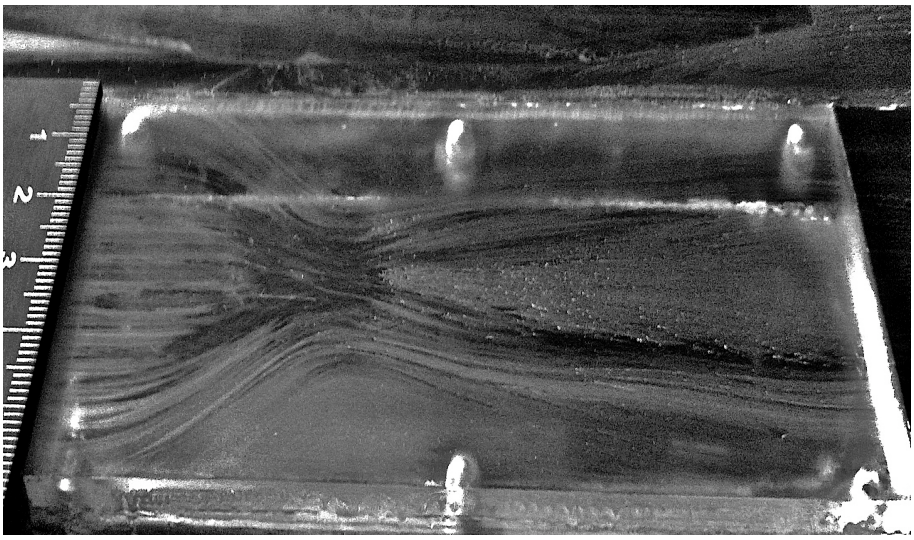

Figure 4.7: Bottom wall oil flow through the UM 3DI-SBLI region. Large corner effects obscure any centerline interaction. Flow from left to right.

the wedge which indicates the inviscid shock location before the upstream influence line diverges from the shock foot. As the oil flow develops, the extent of the interaction reaches further upstream, following the upstream influence line until this flow impinges on the bottom wall. Simultaneous oil flow of the bottom wall, imaged through a plate in the floor, shows the drastic effect that this impingement has on diverting the floor shear stress lines towards the center of the tunnel. Connection of these skin friction lines to the local flow field causing this behavior will be discussed in §5.1, § 5.2, and §6.2.

Previous oil studies by Bookey et al. (2005) in an oblique impinging SBLI indicated a large central separated zone shown in Fig. 4.9. A similar velocity map was confirmed in the PIV studies of Dupont et al. (2005). The significant difference between the our results and these two images requires an alternate explanation.

Examining Figs. 4.6 and 4.8(e) more closely we observe that the line connecting the corner interaction to the leading edge of the wedge is nearly coincident with the upstream influence from the fin-plate SBLI. This makes sense in the SFSC because as

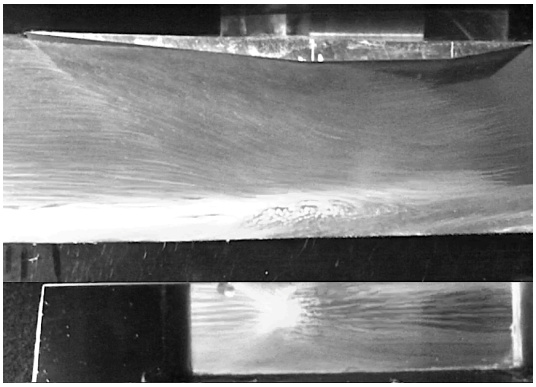

(a) t=0.2s

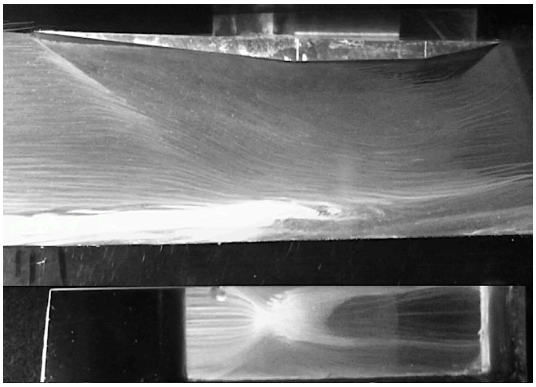

(b) t=0.3s

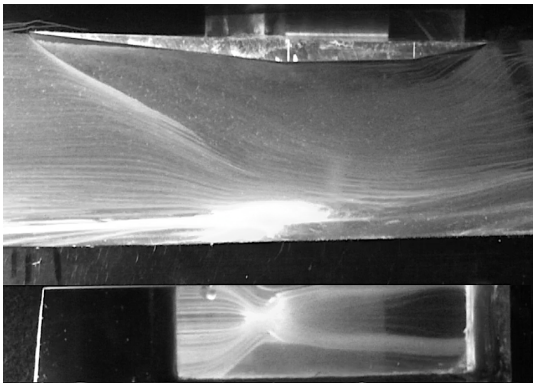

(c) t=0.4s

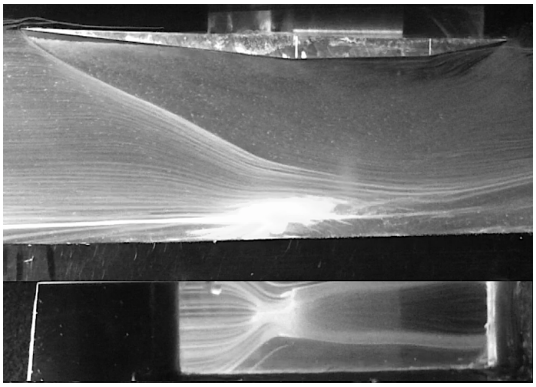

(d) t=0.5s

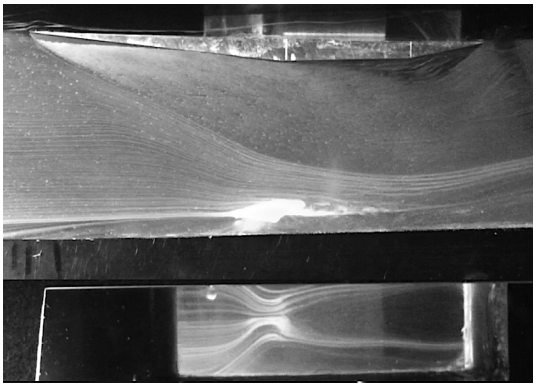

(e) t=0.6s

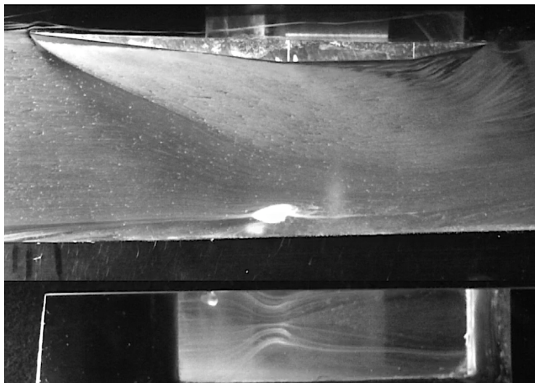

(f) t=3.7s

Figure 4.8: Flow topology sequence. Shock forms and produces vorticity which concentrates under the shock foot on the sidewall. Along the centerline, flow convergence towards the centerline prevents an oil flow visible stagnant flow region. A horseshoe vortex structure appears in the wake, collecting oil and sweeping it downstream. Flow reattachment on the centerline downstream accounts for the lack of oil in the downstream region. Slight visual asymmetry in the bottom wall is attributed to facility effects and uneven application of oil.

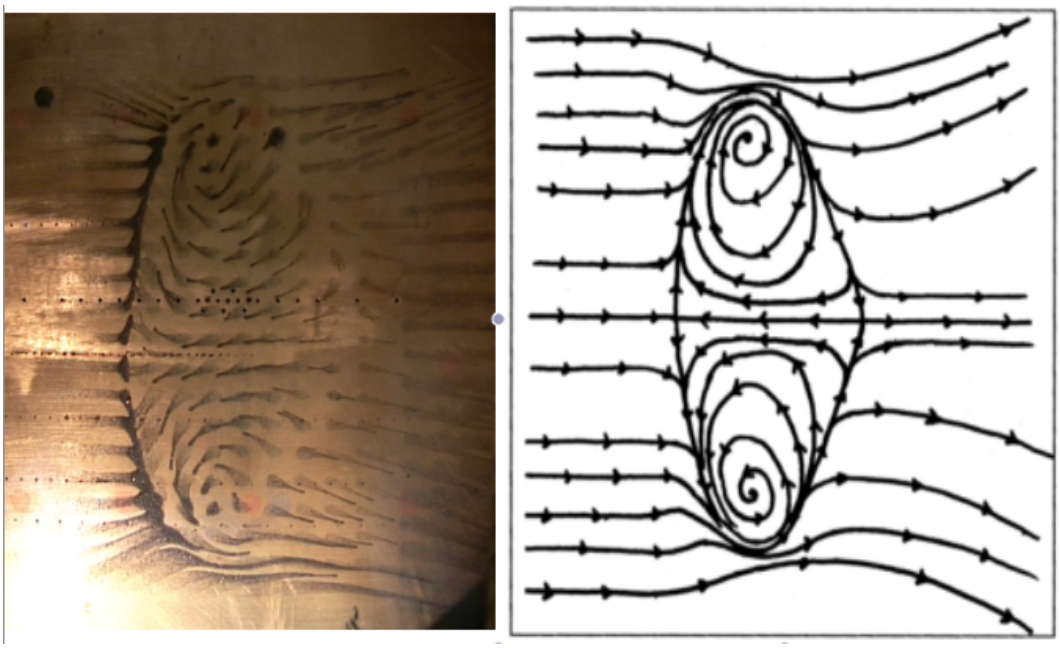

Figure 4.9: Bottom wall oil flow through the oblique shock interaction of Bookey et al. (2005) shows a dramatic centerline separation. Flow from left to right.

described in §2.3 a 90 degree corner region is a mathematical singularity, where the local skin friction is always zero. Thus the corner reacts to the incoming separation line as if it were already a critical point, bifurcating the flow and establishing a new flow topology.

Static images after the tunnel shutdown are illustrative of the long time behavior of scavenging by near wall vortex lift-off. The high shear produced by the vortex motion in the foot of the shock on the sidewall causes the oil in the foot region in Fig. 4.6 to be less opaque than the surrounding regions. The image of the bottom wall in Fig. 4.7 shows a large region absent of oil on the bottom wall followed by a diverging horseshoe shape downstream. The interaction regions can be broken into several regions shown in Fig. 4.10.

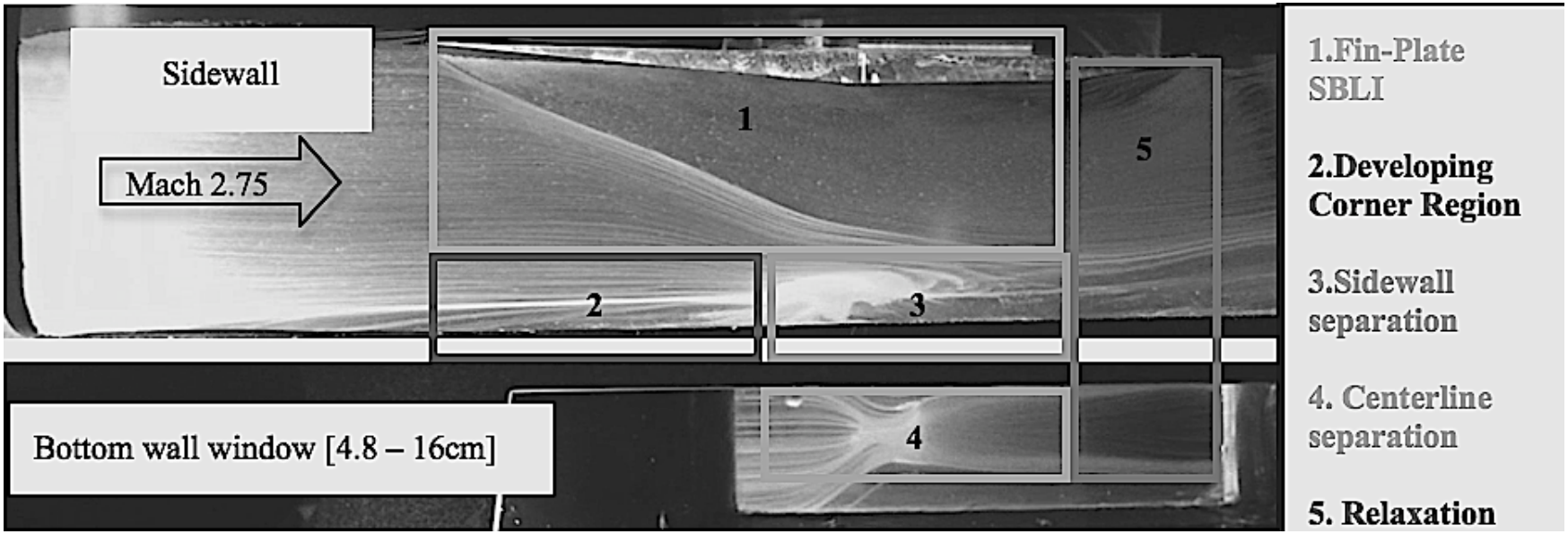

Figure 4.10: 3DI-SBLI region broken into component parts

4.3 Three-dimensional Effects on Pressure

One problem arising in realistic inlet geometries, but commonly ignored by many approaches, is the effect of flow field three-dimensionality. The current experiment adds to our present understanding by visualizing the cause and effect of three-dimensionality in the boundary layer of an oblique shock boundary layer. In this case, the impact of the corner region in this geometry is significant. Figure 4.11 shows the relative position along the centerline of the local pressure rise to the location of the onset of upstream influence. Upstream influence is roughly the distance upstream that the subsonic line first begins to deviate from the wall and is marked by the beginning of the pressure rise, which is presumed to be nearly coincident with the origin of the reflected shock foot. For our current study there are marked differences from the nominally 2D interactions studied by Reda and Murphy (1973b). Although, previous results by Lapsa (2009) taken with a 3/5 span wedge appear to closely approximate the 'two-dimensional' interaction.

At the nozzle exit the free stream pitot pressure was recorded. Table 4.1 contains the values of the recorded pressure data. From the pitot pressure, a free stream Mach number was determined. However, the static pressure measured at the sidewall of the tunnel was not coincident with the probe on the centerline and so the Mach number has uncertainties due to unknown pressure gradients that occur between the sidewall and the centerline of the tunnel. Furthermore, the total pressure loss through the screens in the upstream plenum remains unknown. The estimates given are to be considered preliminary.

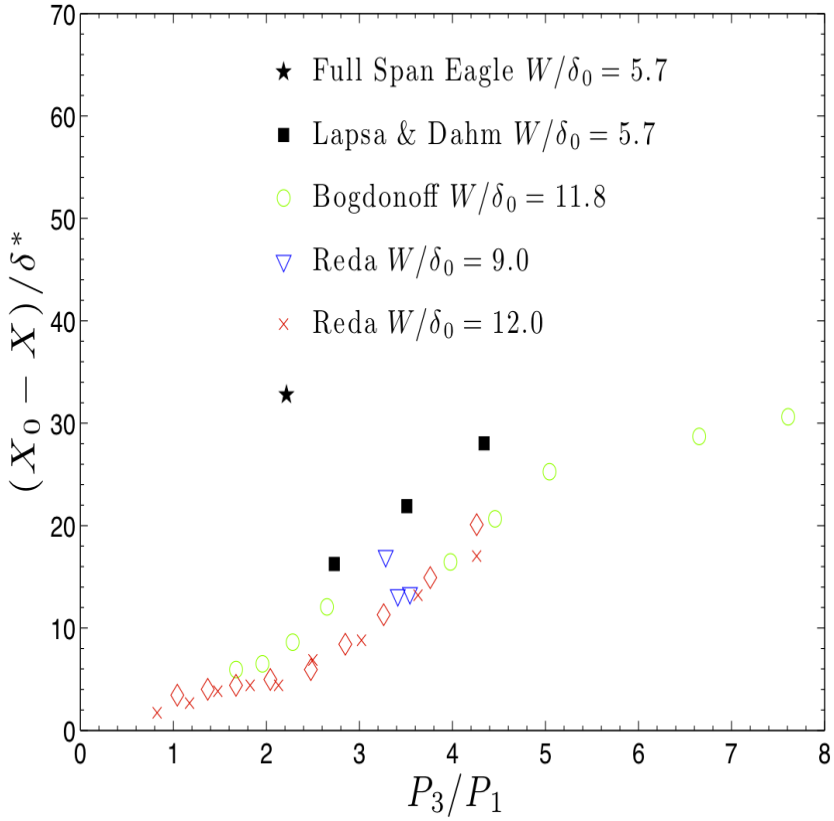

Figure 4.11: Wall static pressure versus non-dimensional upstream distance for different values of tunnel width. Current experiment in low aspect ratio tunnel departs significantly from previous trends in wider tunnels.

Room Barometric Pressure	98.2 kPa
Tunnel Pitot Pressure	88.47 kPa
Local Wall Static Pressure	9.737 kPa
Mach Number Estimate	2.59

Table 4.1: Estimated Mach number based on Pitot measurement at x=-144 mm on the tunnel centerline.

CHAPTER V

Streamwise Data

The data in this chapter was recorded in the streamwise vertical and horizontal planes. Other than Helmer (2011) there is no data for SBLI located near a sidewall boundary layer or a corner. Thus, the primary focus of this section is elucidating these off-centerline and corner interaction features. Since an exhaustive amount of data has been collected, only select planes will be presented and discussed in the body of the thesis. To review all the streamwise data, their gradients, and turbulence quantities in contour and profile form please see Appendices B and C.

5.1 Vertical Planes

Three planes of data are recorded in the vertical direction. The field of view of the vertical planes was somewhat constrained by the optical access in the floor of the wind tunnel. SPIV data was recorded at the centerline, 8 mm off centerline(21 mm from the wall) and 12 mm off centerline (17 mm) from the wall. The locations of each plane are listed in Table 5.1 along with the interrogation window size and pictured schematically in Fig. 5.1. The planes are labeled SV designating they are oriented with the streamwise vertical direction and the numbering scheme starts closest to the centerline wall, with increasing numbers indicating movement towards the sidewall.

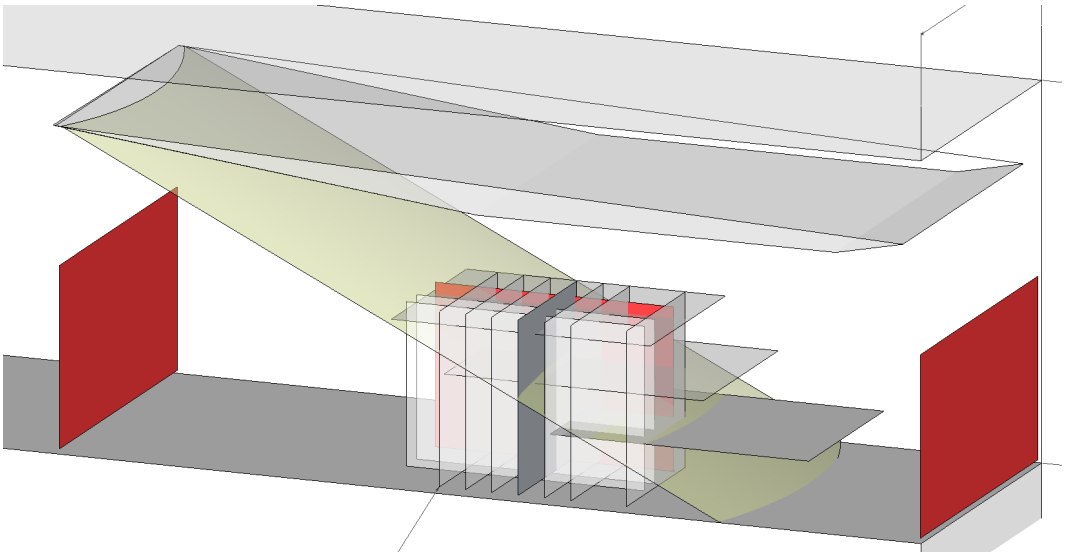

Figure 5.1: Scale drawing of the location of the data planes relative to the shock generator and the inviscid shock location (yellow). Table 5.1 provides labels and locations of the three vertical planes shown in this section. SV1 is on the centerline with increasing values (SV2, SV3) approaching the sidewalls.

Image Plane	x	y	z	Δx	Δy	Δz
SV1	70-120	1- 27	28	0.49 mm	0.49 mm	1.5 mm
SV2	57-100	1- 27	21	0.49 mm	0.49 mm	1.5 mm
SV3	59-106	1- 27	17	0.49 mm	0.49 mm	1.5 mm

Table 5.1: Vertical Image Plane Locations and PIV interrogation window size. $x = 0$ at Shock Generator Leading Edge (for reference geometry please see Appendix A.)

The locations SV2 and SV3 move upstream in the streamwise direction(not pictured) to better capture the upstream motion of the shock foot visible in the oil flow.

5.1.1 Three-Dimensionality of the Interaction

The three-dimensionality observed in the streamwise planes is fairly dramatic in comparison to the Schlieren pictures from the previous section, but consistent with the the flow description hinted at by the oil flow. Fig. 5.2 shows each component of velocity, a computed normal strain (a good indicator of shock location) and the

streamwise vorticity across the centerline image plane, while Fig. 5.3 displays the root mean squared velocity fluctuations as well as one component of the Reynolds Stress (*u'v'*) and the turbulence kinetic energy (for full derivations of these derived quantities from PIV see Lapsa (2009)). Trends discussed between the two planes displayed here are consistent with the intermediate data plane, the presentation of which occurs in Appendix B. As with previous studies, significant reversed flow is measured instantaneously under the shock intersection, but reversed flow does not appear in the time average.

The centerline view shown in Figs. 5.2 and 5.3 is substantially similar to previous interactions in the Michigan supersonic wind tunnel (Lapsa, 2009) and representative of many features which will be discussed throughout. For example, in Fig. 5.2(a) the contours of streamwise velocity, displays qualitative thickening of the boundary layer and it's relaxation downstream of the interaction. Figure 5.2(b) helps to visualize the incoming and reflecting shock location as strong negative(compressive) strain rates, while an expansion fan downstream of the shock intersection is represented by the positive strain. The foot of the reflected shock is most visible in the vertical velocities of Fig. 5.2(c). The transverse component of velocity

Figure 5.4 presents data from the flow off centerline at the 17 mm location. The shock foot moves progressively upstream as you move away from the centerline of the interaction. The shock foot is visualized in these planes by the normal strain rate, S_{yy}. In the centerline, the shock foot location is estimated to be at $x = 76\,mm$, while in the $z = 17\,mm$ plane, this location has advanced to $x = 70\,mm$. This relative motion is in agreement with the oil flow data from Chapter IV which shows the skin friction line of separation moving upstream as the corner is approached from the centerline.

Patterns emerge from the data as the interaction varies across the span. The magnitude of flow turning in the vertical direction is strongest at the centerline and weakens progressively towards the sidewall. In Fig. 5.4, ahead of the reflected shock foot there is spanwise flow towards the centerline in the entire boundary layer. By the shock reflection however, this spanwise flow has lifted off the wall and in the bottom portion of the boundary layer has reversed direction. This pattern of flow is consistent with the horseshoe vortex pattern diverging from the centerline downstream of the interaction in Fig. 4.7.

Because of the strong gradients through these regions, it is reasonable to assume that such velocity patterns are indicative of strengthening of the streamwise vorticity in the boundary layer under the shock foot. In particular, it is interesting to see the local value of the Reynold's shear stress in each of the planes. In the two-dimensional limit, the shear stress goes to zero at a point of separation. In Fig. 5.3 the Reynold's shear stress transitions from a negative value to a positive one. However, in the mean, no such zero point is notable despite reverse flow occurring instantaneously in the image sequence.

Comparing the streamwise velocity profile along the centerline to a plane $12\,mm$ off centerline in Fig.5.4 and 5.5 makes some of the three-dimensionality visible in the streamwise direction. The shock foot location moves upstream as the sidewall is approached. Quantitatively the motion is significant. For a $10\,mm$ movement from the centerline, the front edge of the interaction region – located by the first significant vertical flow region – moves from approximately $79\,mm$ to $69\,mm$ (an equivalent $10\,mm$ shift). The relative strengths of the vertical flow also changes considerably, as does character downstream of the shock interaction location. The contours along the centerline show much stronger vertical velocities,

Three-dimensionality is also visible in the significant changes to the cross flow, U_z, towards the centerline is apparent ahead of the reflected shock as well as behind the incident shock. In contrast, the opposite is true behind the reflected shock location. The spike in boundary layer thickness (as determined by vorticity diffusion/convection) is also significantly more pronounced at the centerline than in the $17\,mm$ location. This can be attributed to the difference in magnitude of the wall normal flow induced at the centerline compared to the reduced quantity in this location. In the fluctuating quantities, there is a notable jump in the w' component as the sidewalls are approached.

The overall trend from these velocity profiles is the trend to push flow away from the corner and towards the centerline. This flow structure concentrates turbulence kinetic energy at the centerline location which invigorates the shape parameter, H, along the center line helping to prevent separation.

5.1.2 Vorticity, Vortex Lines and Secondary Flows

Another method of visualization for PIV uses the data to calculate streamlines. The streamline analysis allows us to investigate for topological features in the flows themselves. In this case, rather than image the streamlines however, we are interested in imaging the 'vortex lines' since the surface vorticity is what drives the skin friction lines. To produce a visualization of a vortex line, we modify the traditional streamline equation by subtracting an average 'two-dimensional' flow component $[U_{avg}\, V_{avg}]$ This visualization method was pioneered by PIV developer Ron Adrian to visualize vortex cores relative to a fast moving free stream. The 'vortex line' equation looks like:

$$\frac{du}{u - U_{avg}} = \frac{dv}{v - V_{avg}} \tag{5.1}$$

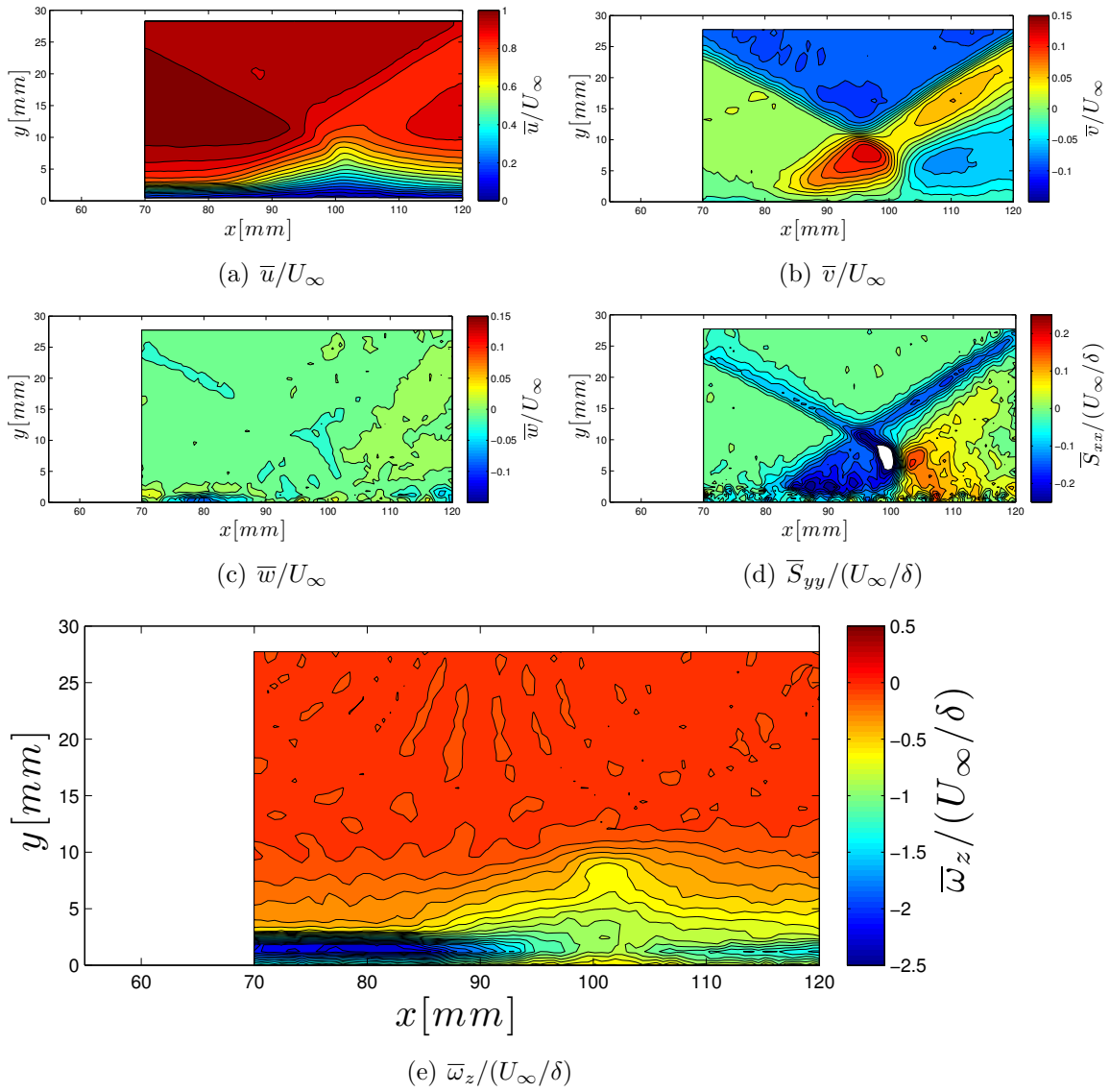

(a) $\overline{u}/U_\infty$

(b) $\overline{v}/U_\infty$

(c) $\overline{w}/U_\infty$

(d) $\overline{S}_{yy}/(U_\infty/\delta)$

(e) $\overline{\omega}_z/(U_\infty/\delta)$

Figure 5.2: Velocities: streamwise(a), vertical(b), transverse(c), computed streamwise normal strain(d) and spanwise vorticity(e) along z=28 mm (centerline plane SV1.) Flow is left to right.

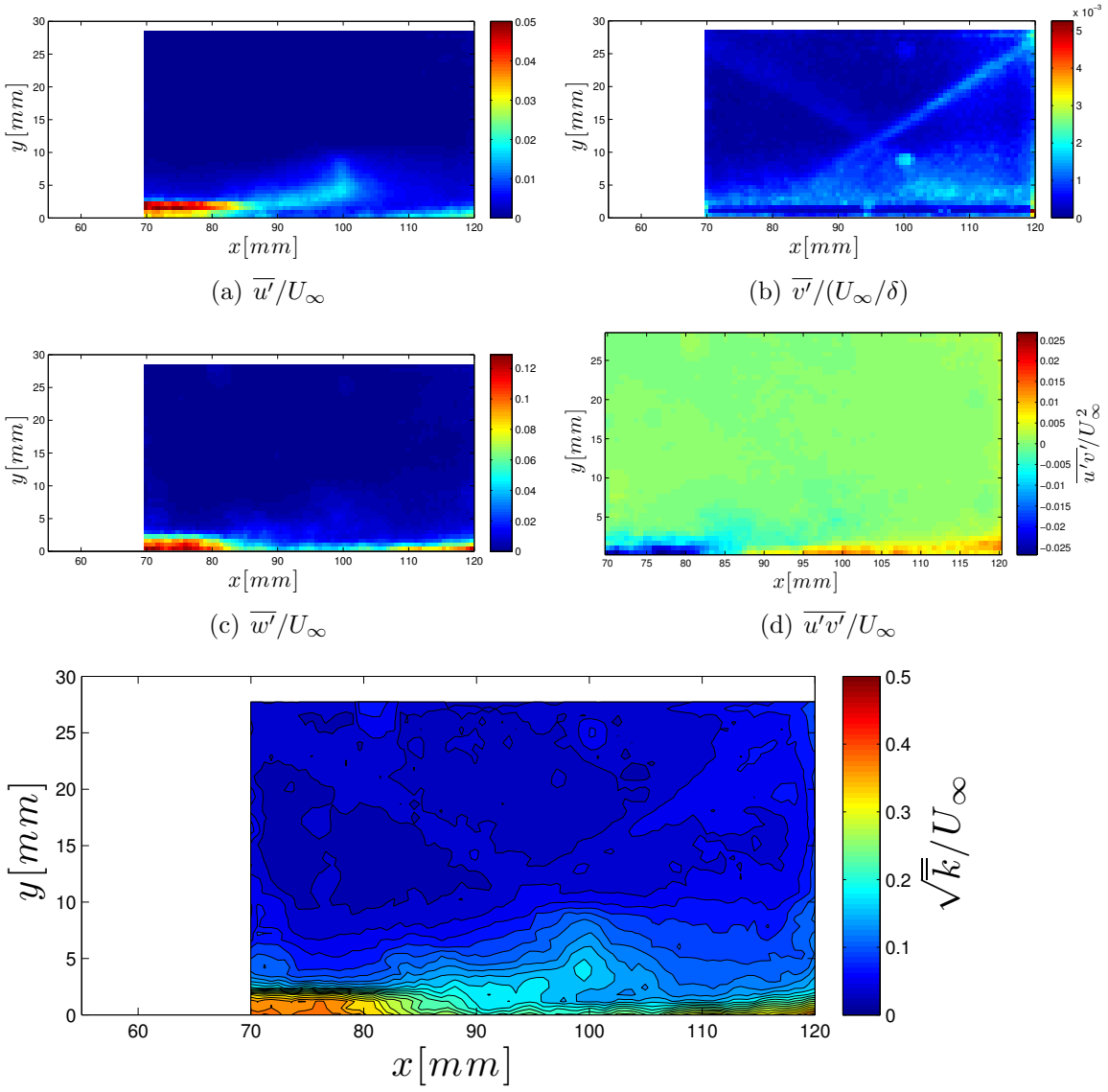

(a) $\overline{u'}/U_\infty$

(b) $\overline{v'}/(U_\infty/\delta)$

(c) $\overline{w'}/U_\infty$

(d) $\overline{u'v'}/U_\infty$

(e) $\overline{k}/(U_\infty)$

Figure 5.3: RMS Velocity fluctuations: Streamwise(a), vertical(b), transverse(c), Reynolds stress(d) and turbulence kinetic energy(e) along z=28mm (centerline plane SV1.) Flow is left to right.

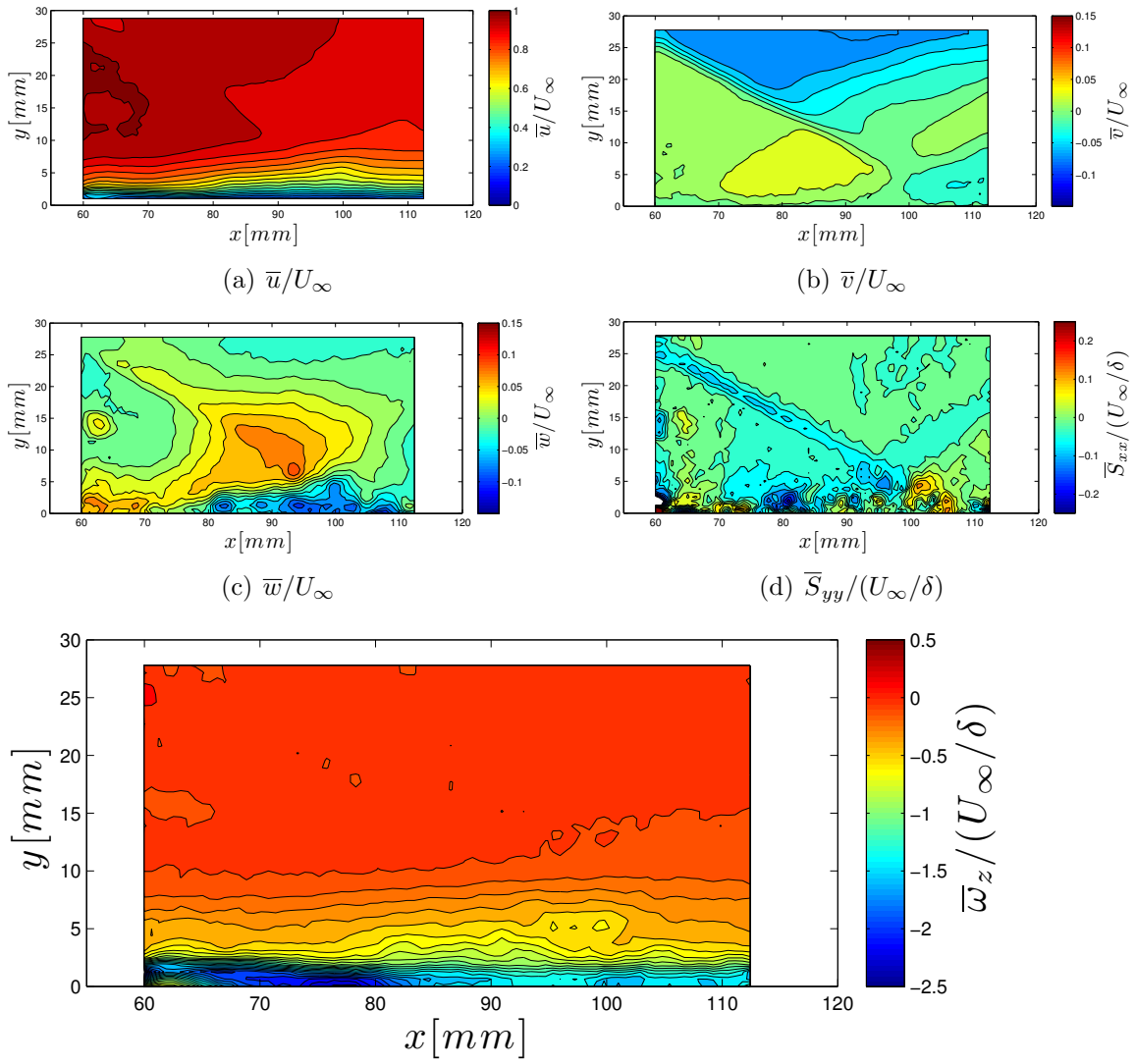

(a) $\overline{u}/U_\infty$

(b) $\overline{v}/U_\infty$

(c) $\overline{w}/U_\infty$

(d) $\overline{S}_{yy}/(U_\infty/\delta)$

(e) $\overline{\omega}_z/(U_\infty/\delta)$

Figure 5.4: Velocities: streamwise(a), vertical(b), transverse(c), computed streamwise normal strain(d) and spanwise vorticity(e) at z=17mm (data plane SV3). Flow is left to right.

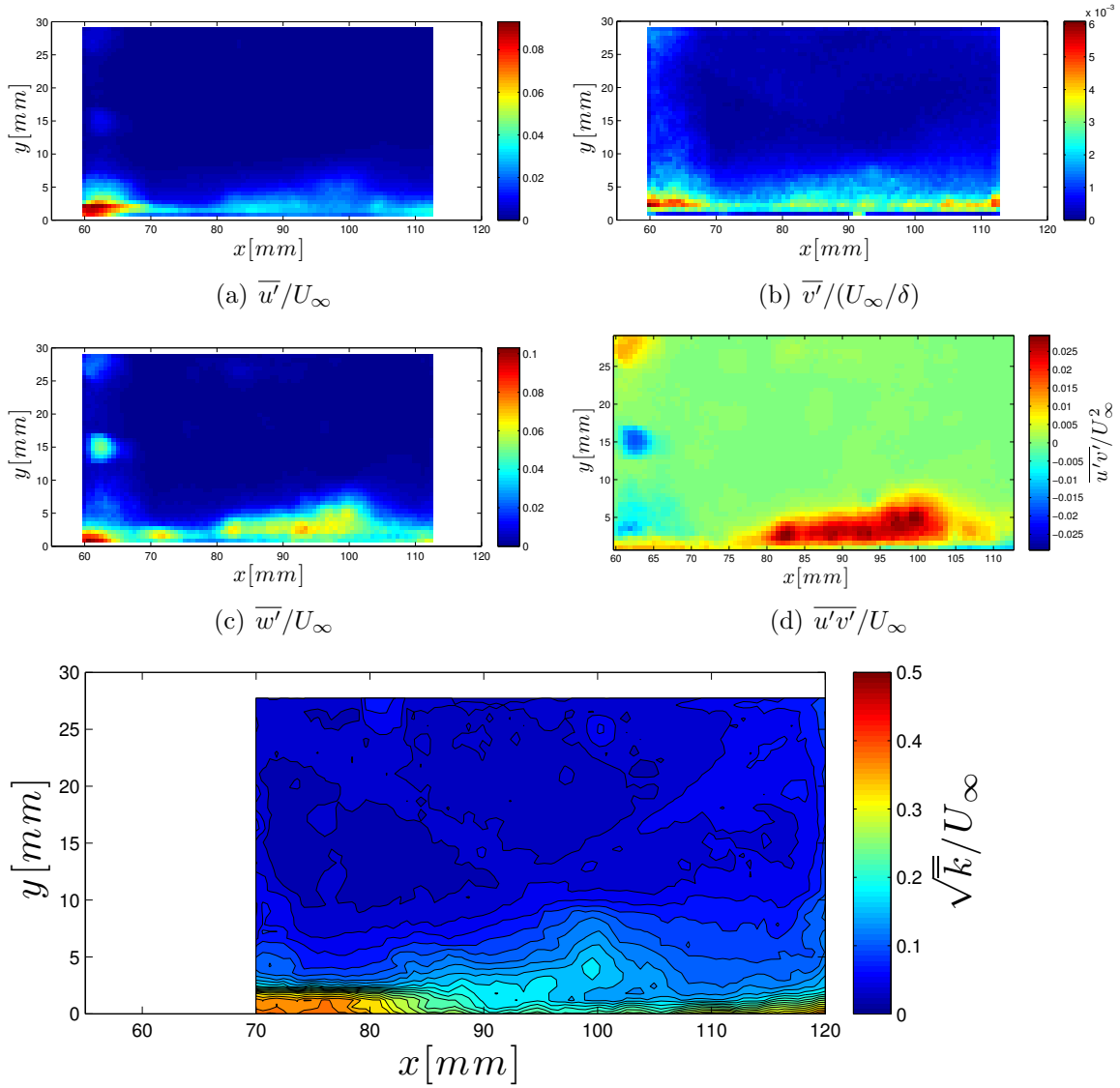

(a) $\overline{u'}/U_\infty$

(b) $\overline{v'}/(U_\infty/\delta)$

(c) $\overline{w'}/U_\infty$

(d) $\overline{u'v'}/U_\infty$

(e) $\overline{k}/(U_\infty)$

Figure 5.5: RMS Velocity fluctuations: Streamwise(a), vertical(b), transverse(c), Reynolds stress(d) and turbulence kinetic energy(e) at z=17mm (data plane SV3).

An instantaneous picture of the vortex lines is shown in Fig. 5.6. Note the presence of a large subsonic region (dark blue), and with several coherent vortex structures upstream of the shock foot. Also, in such a framework, the shockwaves are visible as lines of convergence of the vortex lines, much like the lines of separation were lines of convergence in the skin friction picture.

Figures 5.7, 5.8, and 5.9 are the vortex lines of the ensemble averaged images. The strongest vortex structure occurs at the centerline, with progressive stretching of the interaction structure causing the vortical region to elongate as the sidewall is approached.

Vorticity and vortex lines are excellent candidates for understanding three-dimensional flows. The traditional definitions of boundary layer thickness are dependent on many simplifying two-dimensional assumptions. If instead a vorticity threshold criterion is applied, the physical mechanism of the boundary layer, which functions to diffuse vorticity into the flow, can be better visualized in a three-dimensional flow.

5.1.3 Summary

Through out the vertical interactions, the following general trends are apparent:

1) Symmetry enforced at the centerline diminishes the out of plane component, but this component is roughly equal in magnitude to the vertical component for both planes away from the centerline downstream of the interaction.

2) In accordance with the bottom wall oil images, the shock foot moves upstream as the sidewall is approached.

3) The wall normal strain rate, S_{yy}, best captures the position of the shockwaves in the vertical image plane.

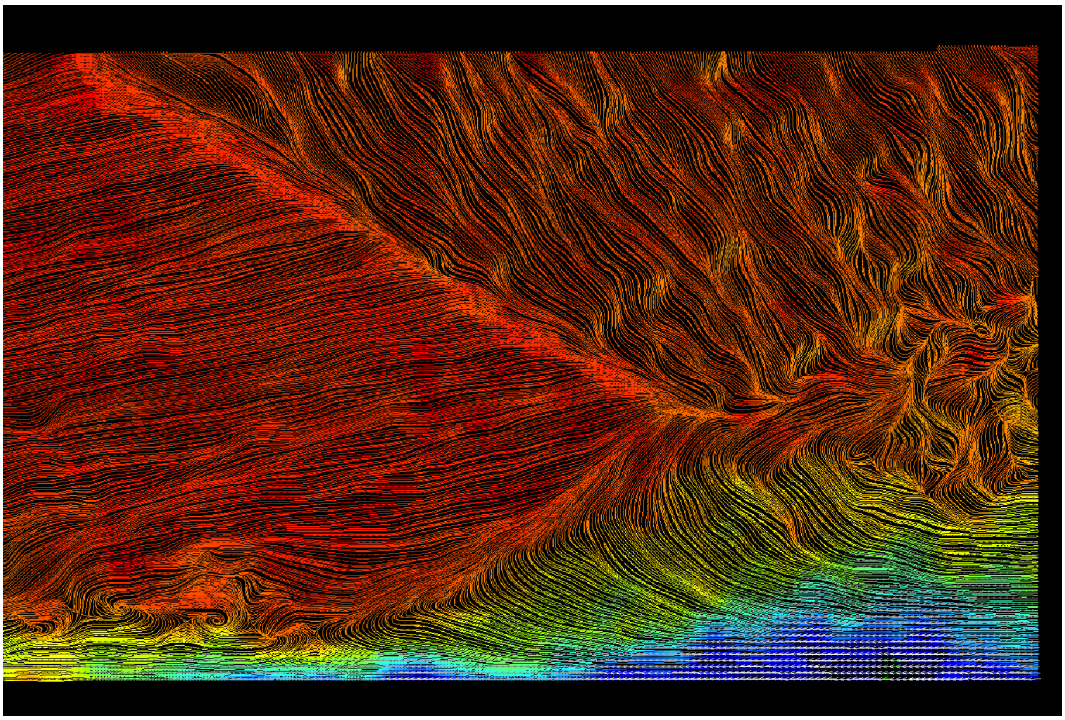

Figure 5.6: Instantaneous 'vortex' lines from SV1. The ensemble average streamwise velocity has been subtracted from this image to allow for relative motion in the vertical plane to be comparable to the horizontal motion. Convergence of lines indicates shock waves. Upstream of the interaction an individual vortex is visible in the boundary layer.

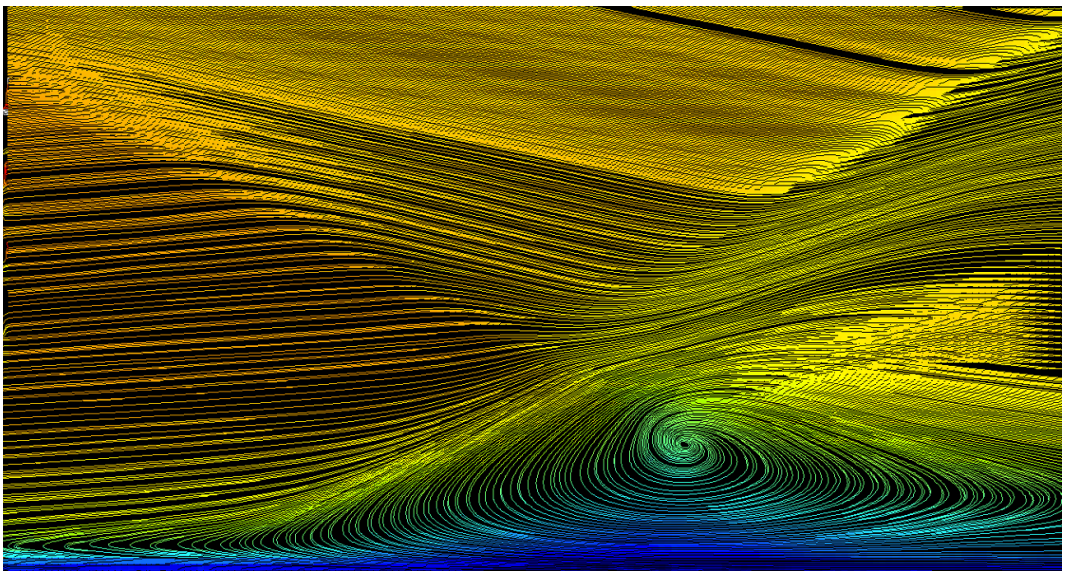

Figure 5.7: Vortex lines of the ensemble field at the centerline (SV1). The average streamwise velocity has been subtracted from the images to allow for relative motion in the vertical plane to be comparable to the horizontal motion.

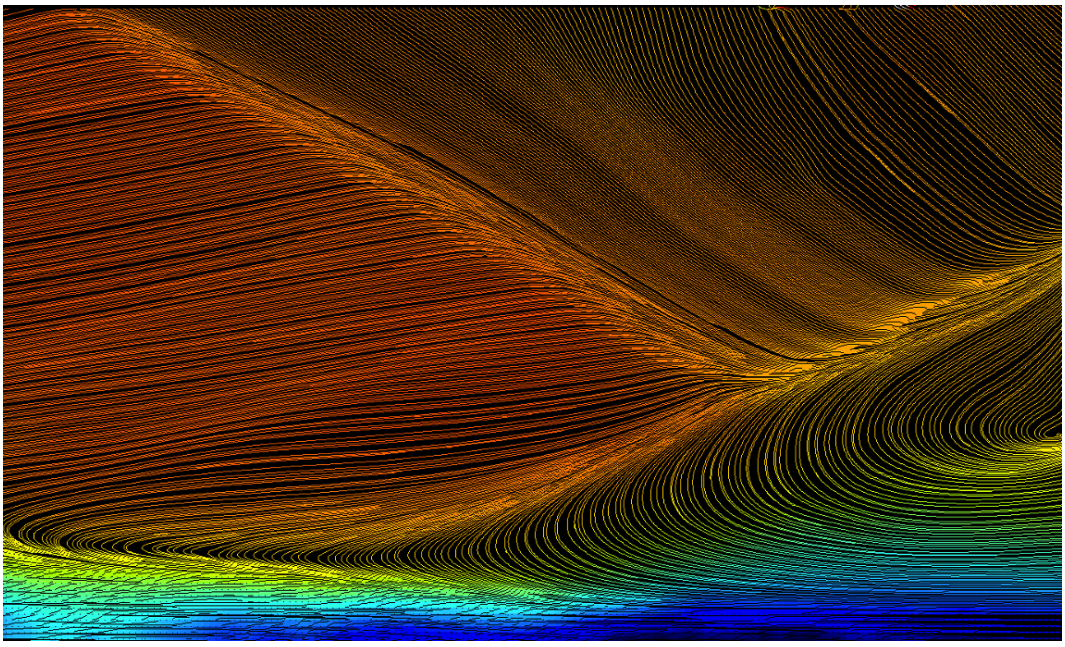

Figure 5.8: Vortex lines at $z = 21\,mm$ (SV2). The average streamwise velocity has been subtracted from the images to allow for relative motion in the vertical plane to be comparable to the horizontal motion.

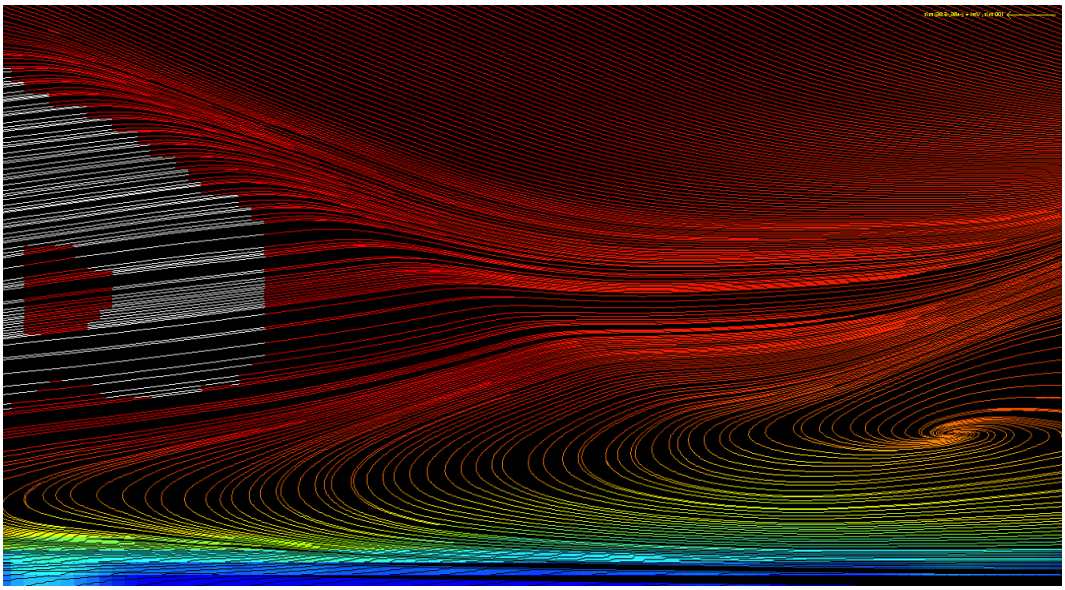

Figure 5.9: Vortex lines at $z = 17\,mm$ (SV3). The average streamwise velocity has been subtracted from the images to allow for relative motion in the vertical plane to be comparable to the horizontal motion.

4) Streamwise vorticity, ω_z, is strengthened through the interaction.

5) In a flow where no single value of 'free stream velocity' can be defined, the boundary layer height can be better assessed by considering a vorticity threshold.

5.2 Horizontal Planes

Three planes of data are recorded in the horizontal direction. The locations of each plane are listed in Table 5.2 and pictured schematically in Fig. 5.10. The planes are labeled SH for 'streamwise horizontal' and the numbering scheme starts closest to the bottom wall, with increasing numbers indicating movement away from the wall. The locations are offset in the streamwise direction to capture the incoming shock in the front half of the PIV plane. Data from the horizontal planes is used to quantify the three-dimensionality of interaction and how the flow interactions from the sidewall impact the impinging shock on the bottom wall.

5.2.1 Three-Dimensionality of the Interaction

As in the previous section, each figure will present each component of velocity, a computed normal strain (a good indicator of shock location) and the vorticity. For more detailed computed quantities of interest, please see Appendix C. (for full

Image Plane	x	y	z	Δx	Δy	Δz
SH1	90-130	9.5	13-44	0.43	1.5	0.43
SH2	78-125	19	13-42	0.43	1.5	0.43
SH3	59-106	28.5	13-44	0.43	1.5	0.43

Table 5.2: Horizontal Image Plane Locations in mm. $x = 0$ is coincident with the shock generator leading edge (for reference geometry see Appendix A.)

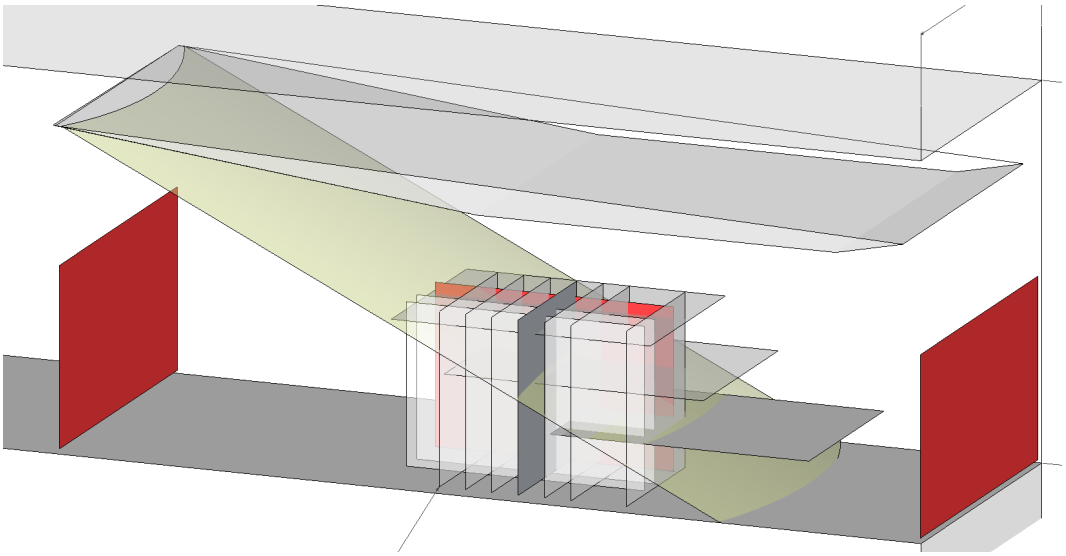

Figure 5.10: Scale drawing of the location of the data planes relative to the shock generator and the inviscid shock location (yellow). Table 5.2 provides labels and locations of the three horizontal planes. SH1 is closest to the wall, while SH3 is furthest.

derivations of these derived quantities from PIV see Lapsa (2009)). Trends are discussed for quantities in all planes. No reversed flow is seen due to the distance from the walls in every direction, however, the horizontal planes are excellent for visualizing symmetry about the tunnel centerline.

Figures 5.11(a), 5.12(a,b,c) and 5.13(c) all display symmetry in the well resolved in plane components of velocity and clear development of three-dimensionality is present in all three planes generated by the impinging shock, but largely eliminated by the reflected shock in the downstream portion.

Although starting relatively mild, such as In Fig. 5.11(b), the shock curvature is visible in the normal strain, S_{xx}, for all the impinging and reflected shock regions. In Fig. 5.12(b) the excursion from the nominal 'inviscid' impinging shock location at the centerline is estimated to be $10-15\,mm$ upstream and for the reflected shock is close to 20mm further downstream.

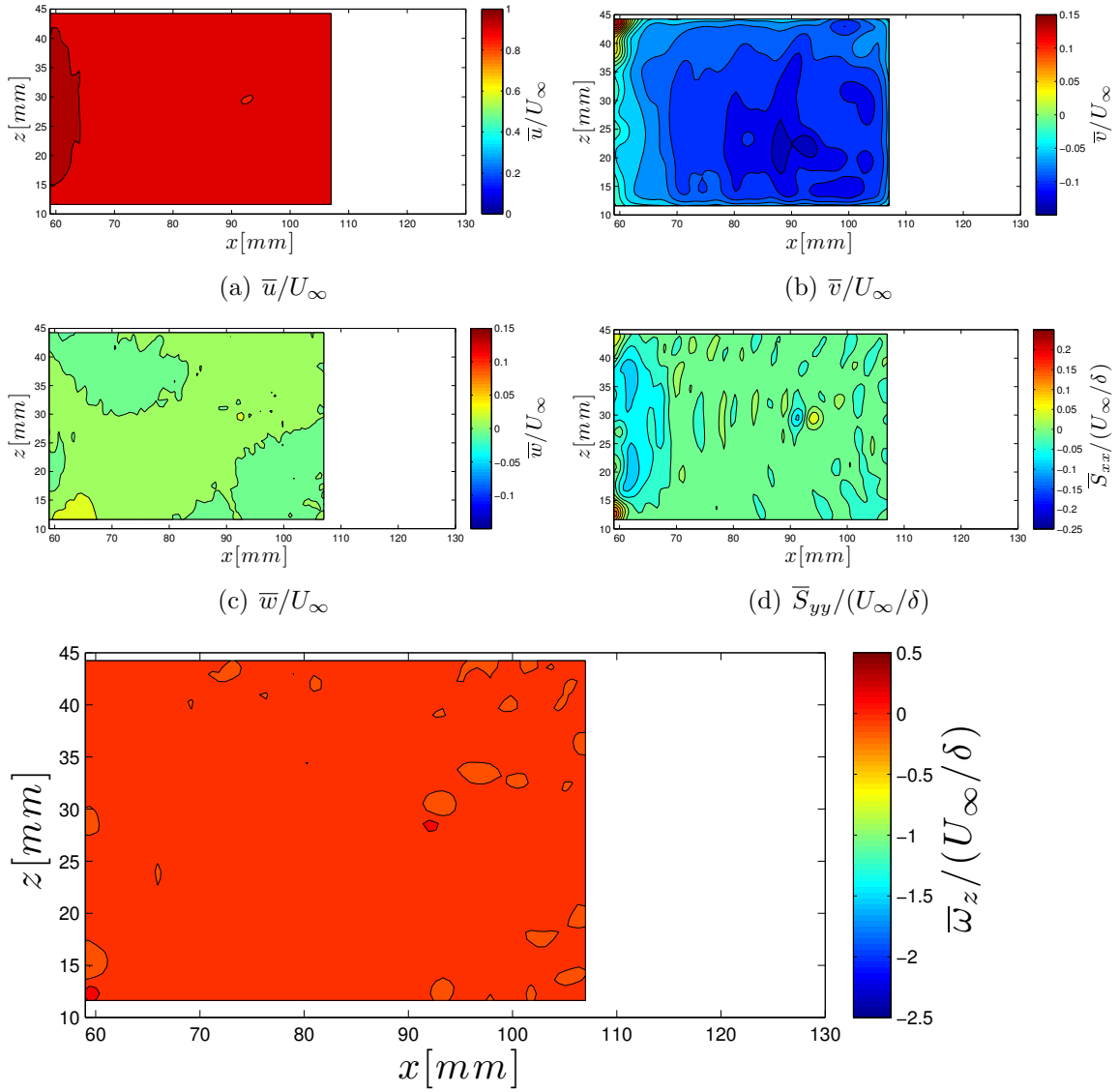

(a) $\overline{u}/U_\infty$

(b) $\overline{v}/U_\infty$

(c) $\overline{w}/U_\infty$

(d) $\overline{S}_{yy}/(U_\infty/\delta)$

(e) $\overline{\omega}_z/(U_\infty/\delta)$

Figure 5.11: Velocities: streamwise(a), vertical(b), transverse(c), computed streamwise normal strain(d) and vertical vorticity(e) at y=28mm (data plane SH3). Flow is left to right, and vertical velocity is positive away from the bottom wall.

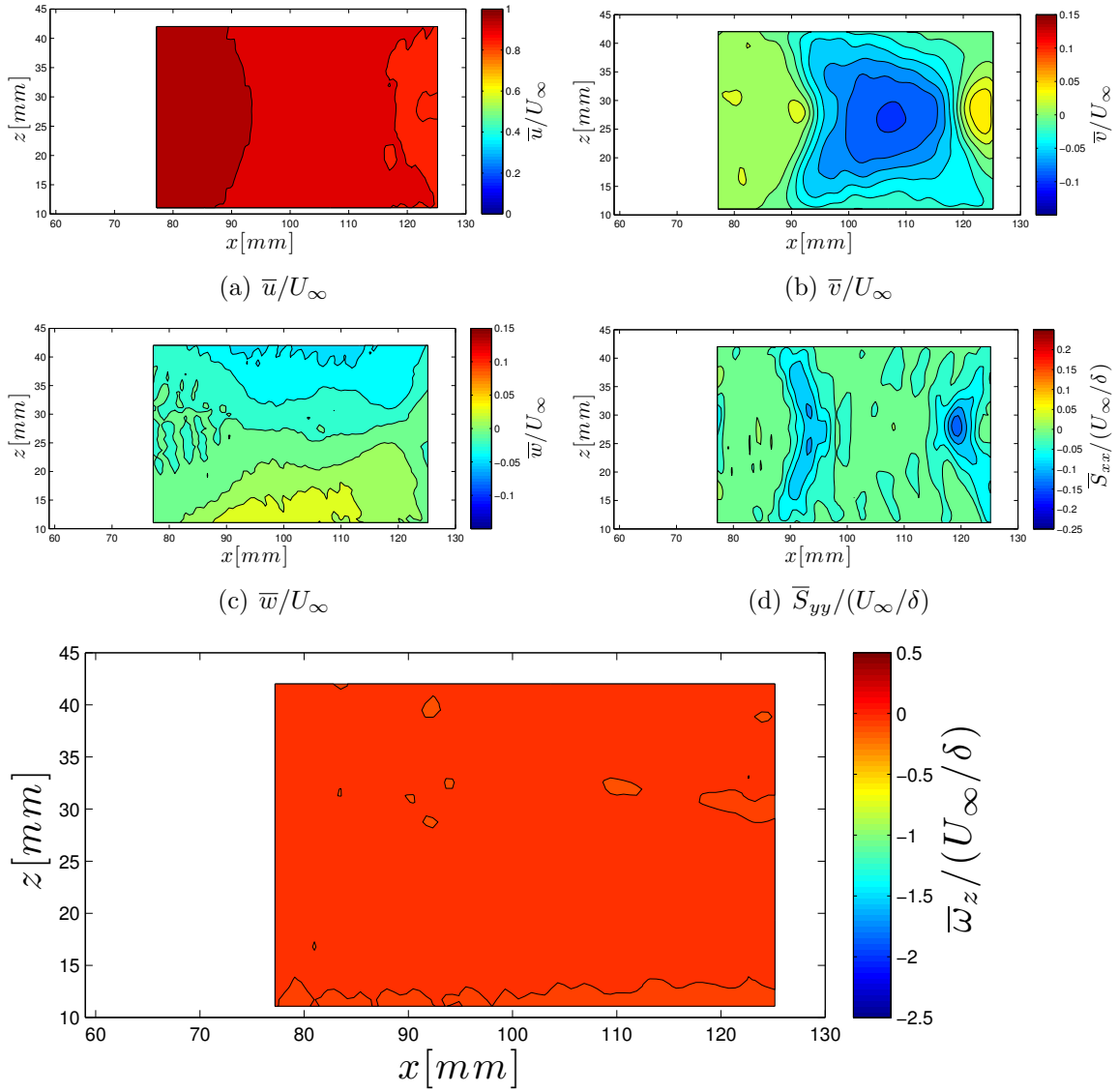

(a) $\overline{u}/U_\infty$

(b) $\overline{v}/U_\infty$

(c) $\overline{w}/U_\infty$

(d) $\overline{S}_{yy}/(U_\infty/\delta)$

(e) $\overline{\omega}_z/(U_\infty/\delta)$

Figure 5.12: Velocities: streamwise(a), vertical(b), transverse(c), computed streamwise normal strain(d) and vertical vorticity(e) y=19mm (data plane SH2.) Flow is left to right, and vertical velocity is positive away from the bottom wall.

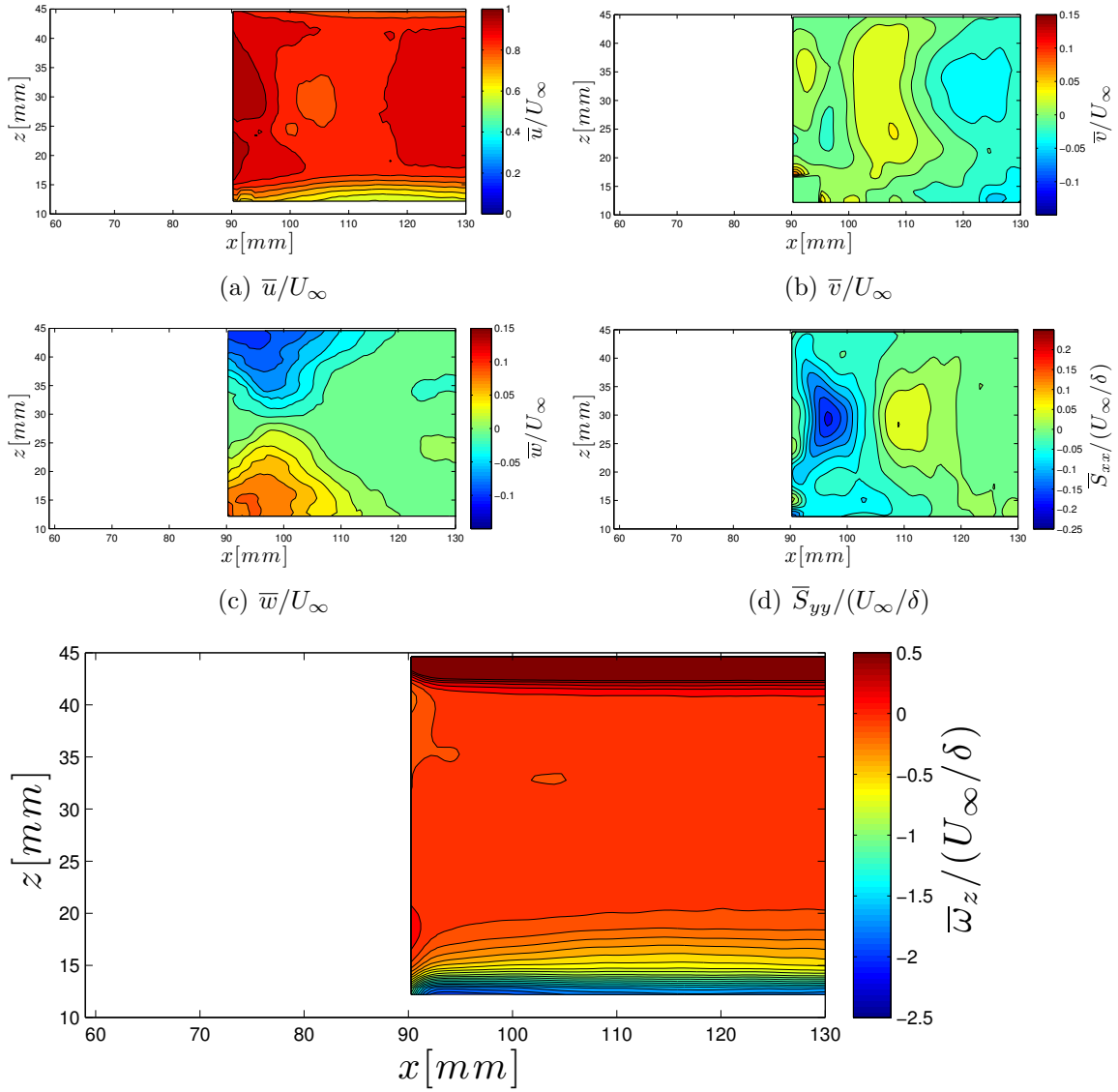

(a) $\overline{u}/U_\infty$

(b) $\overline{v}/U_\infty$

(c) $\overline{w}/U_\infty$

(d) $\overline{S}_{yy}/(U_\infty/\delta)$

(e) $\overline{\omega}_z/(U_\infty/\delta)$

Figure 5.13: Velocities: streamwise(a), vertical(b), transverse(c), computed streamwise normal strain(d) and vertical vorticity(e) y=9.5mm (data plane SH1.) Flow is left to right, and vertical velocity is positive away from the bottom wall.

5.2.2 Vorticity and Vortex Lines

In Tabak and Peake (1982) the authors discuss the extension of the surface flow topology to the velocity field itself. In a follow on article, Perry and Chong (1987) discuss the description of flows using CPT. Although such methods were precursors to today's modern CFD methods, the insight which can be drawn from such reduced order models is still significant. In particular, there are a variety of possible vortex 'skeletons' laid out which could explain the surface streamlines. The purpose of the following section is to draw definitive connections between the flow vortex lines and the surface streamlines.

Visualizing vortex motion in any flow is part art and part science. Ron Adrian's work in vortex motion in the boundary layer successfully employs the method of 'vortex convection' velocity (Elsinga et al., 2010). In this method, a portion of the free stream velocity is subtracted to make the relative velocities normal to the wall comparable to the velocity in the plane. This renders visible in the vector maps any relative circulation, and in particular vortex centers. Such a change of coordinates is referred to as 'Galilean invariance'.

In the horizontal plane above the boundary layer in Fig. 5.14, a vortex structure is apparent upstream and above the interaction zone indicating a local flow separation due to the shock interaction along the sidewall. As the bottom wall interaction is approached, the reflected shock enters the field of view along the downstream edge. At this height, shown in Fig. 5.15 the dominant motion is towards the centerline an no coherent vortex structure is apparent in the ensemble average data. Closest to the bottom wall boundary layer, the vortex motion in Fig. 5.16 displays a pattern of nodal separation and two downstream saddle points, confirming the SFSC that the reflected shock motion at the centerline is produced by a secondary separation.

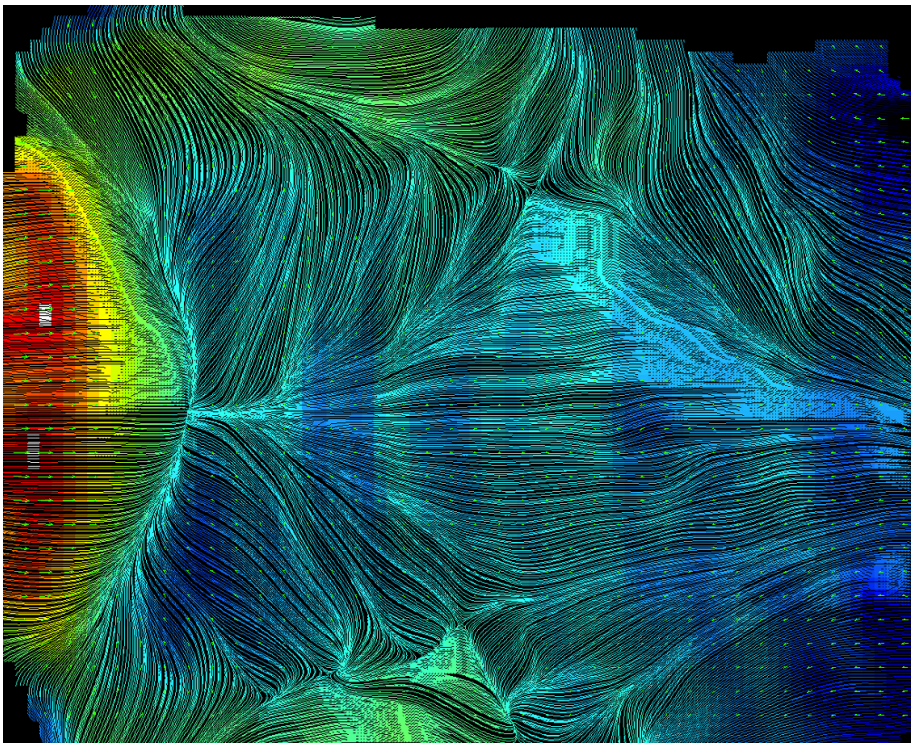

Figure 5.14: Vortex lines in the y=28mm interaction(SV3). Flow is left to right. Incoming flow(red) displays the significant shock curvature. As the walls are approached, a vortex structure which bends the lines towards the sidewall is visible. The shock curvature produces a node on the left of the image. In the top half a saddle point in the flow is clearly visible. The saddle points symmetric image in the bottom half is less clear.

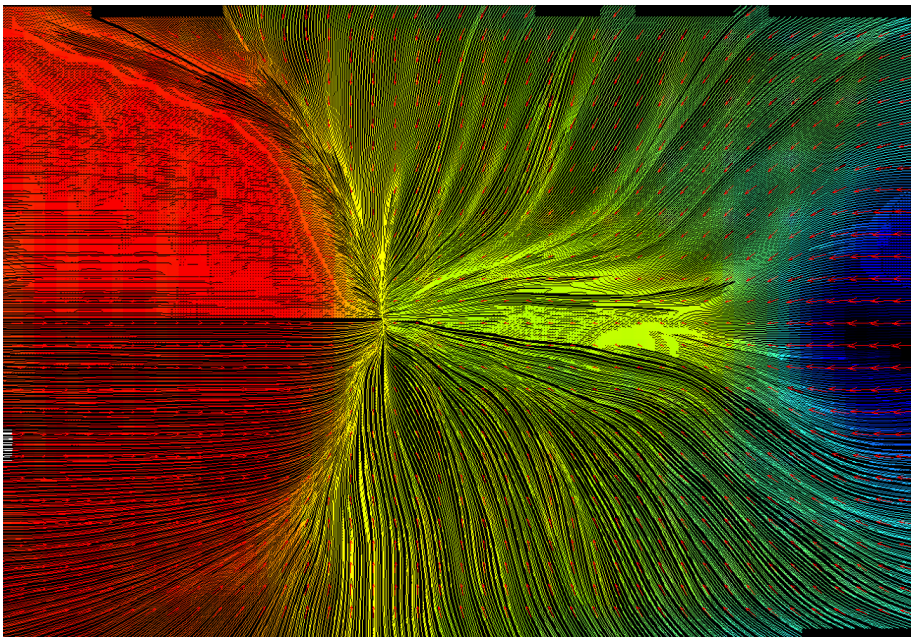

Figure 5.15: Vortex lines in the y=19mm interaction(SV2). Flow is left to right. Upstream and downstream shock curvature are visible in background contour red/blue. No coherent vortex motion is visible this height, but flow symmetry is clear.

5.2.3 Summary

Through out the horizontal plane interaction data the following general trends are apparent.

1) As with the vertical planes, symmetry enforced at the centerline diminishes the out of plane component, but this component is roughly equal in magnitude to the vertical component for both planes away from the centerline downstream of the interaction.

2) The streamwise normal strain rate, S_{xx} best captures the position of the shock-waves in the horizontal image plane (see Figs. 5.11(d), 5.12(d), and 5.13(d). The magnitude of the strain drops by an order of magnitude or more as the side walls are approached. The weakening magnitude of the compressive normal strain explains the two dimensionality in the path integral gradient visualized

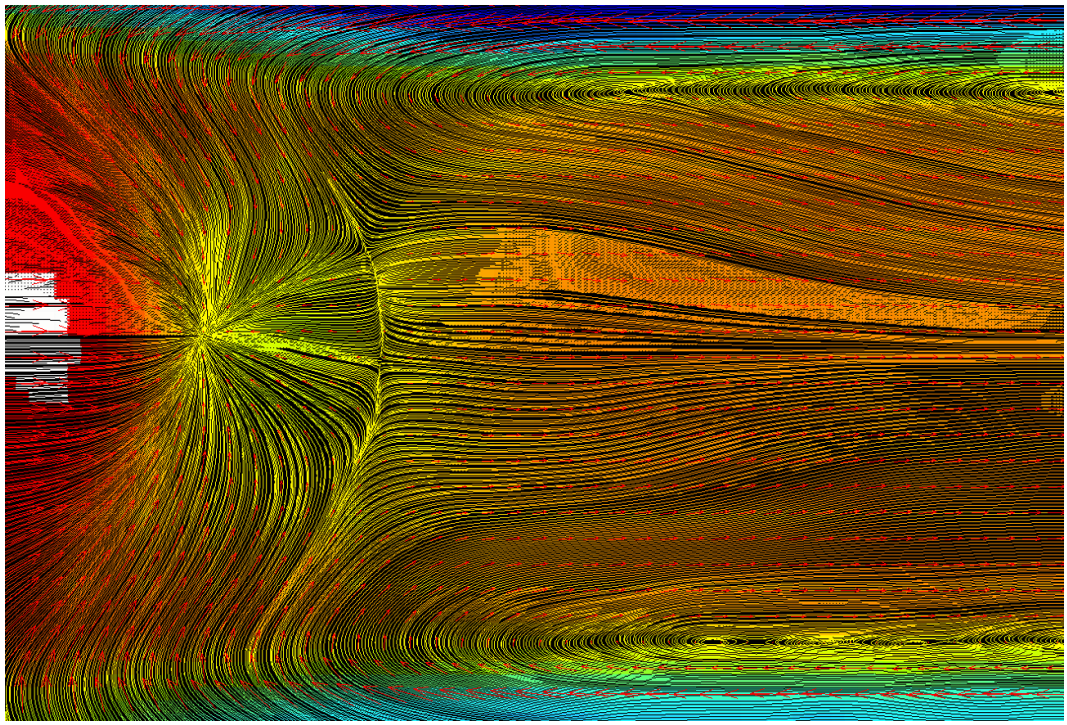

Figure 5.16: Vortex lines in the y=9.5mm interaction (SV1). Nodal separation occurs at centerline with convergence of spanwise velocities. Two downstream saddle points in the flow indicate the location of flow 'reattachment'

by the Schlieren. Since strong contributions occur only near the centerline of the interaction.

3) Due to significant spreading of the velocity gradient, there is no significant amplification of wall normal vorticity, ω_y outside of the boundary layer.

4) In the boundary layer, the vortex lines display features of a secondary separation near the bottom wall, (i.e. a nodal separation followed by two saddle points downstream.)

5.3 PIV Data Limitations

Although a large number of images was taken at each location, the data quality decreases with run time due to glare effects (common to all enclosed PIV flows) from accumulated particles along the sidewalls. To address this issue, only the first 100 images from each run are included in the average. Thus 17 runs constitute each ensemble data set. Previously, flow seeding occurred only in a region local to the measurement plane. However, to ensure consistency between streamwise and transverse PIV planes, the same seeding system was used for all runs. This may unnecessarily limit valid vector detection. For example, some upstream artifacts at the image mid-plane are present in Figs. 5.4, 5.5 and 5.12. These are due to image glare and other similar reflections. Since the vorticity calculation (and any calculations based on gradient quantities) is sensitive to the PIV processing parameters this glare adds additional noise, which shows up in the reported gradients (i.e. S_{xx}.)

The primary drawback to using a stereo method for PIV compared to a standard two-dimensional PIV system is the difficulty of registering and maintaining the posi-

tion of one camera with respect to the other. Errors in camera registration (mapping each camera frame to the lab frame) are responsible for adding bias errors to the measurements. While camera calibration angle increases the RMS error in the out of plane measurement by a factor of up to two to four for camera angles between 15 to 30 degrees off axis (Lawson and Wu, 1997).

Strictly speaking, thicker light sheets than necessary are used for the streamwise plane measurements. This thickening is required for the spanwise planes, is again maintained for the streamwise measurements to keep all elements of uncertainty consistent across measurements when used for comparison. However, this decision leads to some unnecessary volume averaging in the streamwise directions, an additional component of registration error. Stereo-self calibration completed for every image plane shifts the camera registrations an unrecorded amount to account for misalignment between the calibration plate and the laser plane. This indicates that the reported image locations maybe slightly different than those measured. Unfortunately, streamwise data planes were not able to measure the sidewall boundary layer interaction directly because they are constrained by optical access from the bottom of the tunnel. Fortunately, this limitation can be overcome by utilizing data from the spanwise planes, presented next.